



UNIVERSITY OF LEEDS

This is a repository copy of *Axial compressive behaviour and design of concrete-filled wire arc additively manufactured steel tubes*.

White Rose Research Online URL for this paper:

<https://eprints.whiterose.ac.uk/222062/>

Version: Published Version

---

**Article:**

Chen, J., Song, S.-S., Ye, J. [orcid.org/0000-0002-6857-7450](https://orcid.org/0000-0002-6857-7450) et al. (3 more authors) (2024) Axial compressive behaviour and design of concrete-filled wire arc additively manufactured steel tubes. *Structures*, 70. 107495. ISSN 2352-0124

<https://doi.org/10.1016/j.istruc.2024.107495>

---

This is an author produced version of an article published in *Structures*, made available under the terms of the Creative Commons Attribution License (CC BY), which permits unrestricted use, distribution and reproduction in any medium, provided the original work is properly cited.

**Reuse**

This article is distributed under the terms of the Creative Commons Attribution (CC BY) licence. This licence allows you to distribute, remix, tweak, and build upon the work, even commercially, as long as you credit the authors for the original work. More information and the full terms of the licence here:

<https://creativecommons.org/licenses/>

**Takedown**

If you consider content in White Rose Research Online to be in breach of UK law, please notify us by emailing [eprints@whiterose.ac.uk](mailto:eprints@whiterose.ac.uk) including the URL of the record and the reason for the withdrawal request.



[eprints@whiterose.ac.uk](mailto:eprints@whiterose.ac.uk)  
<https://eprints.whiterose.ac.uk/>

# **Axial Compressive Behaviour and Design of Concrete-filled Wire Arc Additively Manufactured Steel Tubes**

Ju Chen<sup>1</sup>, Sha-Sha Song<sup>1</sup>, Jun Ye<sup>1\*</sup>, Guan Quan<sup>1</sup>, Pinelopi Kyvelou<sup>2</sup>, Leroy Gardner<sup>2</sup>

1. Institute of Structural Engineering, Zhejiang University, Hangzhou, Zhejiang, China

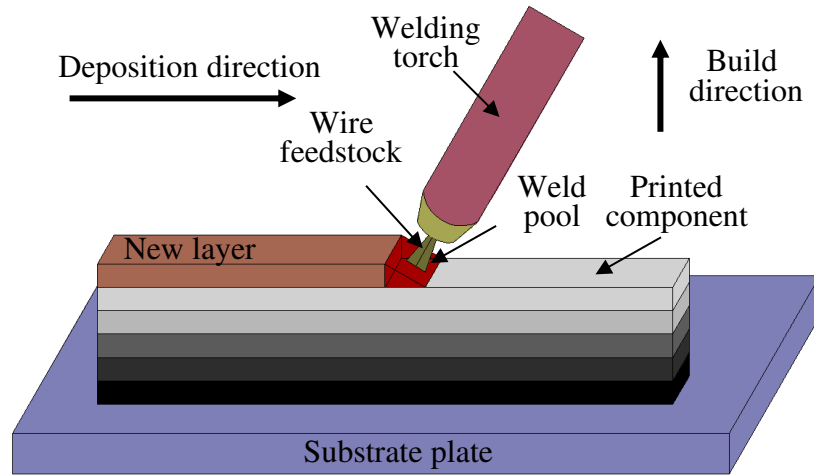
2. Department of Civil and Environmental Engineering, Imperial College London, London, UK

**Abstract:** The axial compressive behaviour of concrete-filled wire arc additively manufactured (WAAM) steel tubular columns is investigated experimentally in this paper. Firstly, the manufacture of a series of WAAM steel plates and tubes is described. The results of tensile testing performed on coupons cut from the WAAM plates, to obtain the mechanical properties of the printed material, are summarised. 3D laser scanning was employed to generate digital models and to capture the geometric features of the WAAM steel test specimens. Concrete was then cast into the WAAM steel tubes, creating a total of nine concrete-filled steel tubular (CFST) specimens of different diameters, thicknesses and lengths that were subjected to compressive loading. The axial compressive load-deformation responses and ultimate loads of the specimens were obtained and the influence of the as-built surface undulations of the WAAM sections was assessed. Comparisons of the test results against existing structural design provisions highlight the need to consider the influence of the weakening effect of the geometric undulations that are inherent to the WAAM process on the structural response of CFST sections, in order to achieve safe-sided strength predictions.

**Keywords:** 3D printing; Axial compressive behaviour; Concrete-filled steel tube (CFST); Experiments; Laser Scanning; Testing; Ultimate load; Wire arc additive manufacturing (WAAM).

## 24 1. INTRODUCTION

25 Recent developments in the directed energy deposition (DED) methods of additive manufacturing  
26 (AM) have led to growing interest in and increasing usage of this technology in the construction sector  
27 [1]. DED methods offer several advantages over other AM methods for constructional applications, such  
28 as relatively low cost, reasonable manufacturing times and essentially unlimited build sizes [2-6].



29

30 Figure 1. Schematic diagram of WAAM process

31 Among the various metal DED technologies, wire arc additive manufacturing (WAAM), which  
32 uses conventional welding technology, coupled with robotic control, is emerging as the method of  
33 choice for large scale applications [1,7-17], and is the focus of the present paper. As shown in Fig. 1,  
34 during the WAAM process, wire feedstock is melted and deposited onto a substrate plate in a layer by  
35 layer fashion. WAAM has the potential to have a significant impact on the construction industry; an  
36 early example of this potential is the MX3D bridge constructed by the Dutch company MX3D  
37 ([www.mx3d.com](http://www.mx3d.com)). With its construction being beyond the scope of current design specifications [18-  
38 21], this novel structure required extensive experimental and numerical research for its safety  
39 assessment. A comprehensive series of experiments was thus conducted, involving material testing  
40 [14,22,23], cross-section testing [24] and full structural testing [25]; numerical simulations were also  
41 carried out [25]. Research into the performance of metal additively manufactured components with a  
42 structural engineering focus has been increasing in recent years [1]. Studies into the behaviour of  
43 structural elements produced by powder bed fusion (PBF) have been reported in [26,27], while

44 investigations into WAAM structural elements have been presented at the material level [14,27-31], the  
45 cross-section level [32,33], the member level [34,35] and the system level [6]. The latter system level  
46 study involved the optimisation [6], testing [36] and environmental impact assessment [37] of a series  
47 of 2 m span WAAM tubular trusses, an example of which is shown in Fig. 2. The use of WAAM for  
48 hybrid construction has also been explored, including recent studies into the structural behaviour of hot-  
49 rolled I-sections strengthened by the addition of WAAM material at the flange tips [38,39].

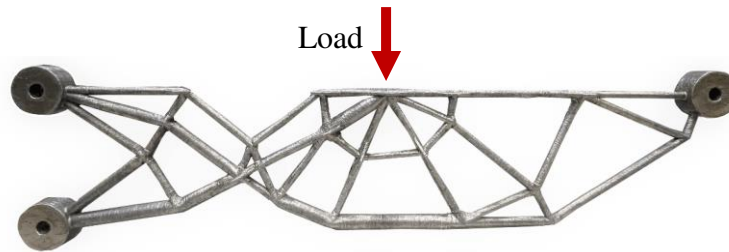


Figure 2. Optimised WAAM tubular truss [36]

50 Concrete-filled steel tubular (CFST) elements are widely used in construction applications [40-47],  
51 such as in arch bridges, high rising buildings and transmission towers. The combined effect of the steel  
52 tube and the inner concrete leads to composite structural members of superior performance relative to  
53 the sum of the component parts [40], with the inner concrete delaying the development of local buckling,  
54 as well as the rise in temperature in the event of a fire, of the steel tube [40,45], and with the steel tube  
55 enhancing the strength and ductility of the inner concrete through confinement action. The steel tube  
56 also eliminates the need of formwork for concrete casting, resulting in fast-track construction. Surface  
57 undulations are a natural characteristic of the WAAM process; in the context of CFST, there undulations  
58 can enhance the interaction between the WAAM steel tube and the inner concrete, and hence improve  
59 the structural performance [48]. Furthermore, unlike CFST members fabricated from conventional steel  
60 tubes that have seam welds running along the length of the members where fracture is often observed  
61 [49,50], the continuously printed ‘hoops’ for which the start and end points of each layer are offset  
62 circumferentially forming the WAAM tubes, are expected to mitigate this issue, resulting in enhanced  
63 ductility [51]. To date, research into the compressive behaviour of CFST members has been limited to  
64 cross-sections comprising conventionally manufactured tubes [41-43,46,47], while the response of  
65 CFST elements with WAAM tubes is still to be investigated. Seeking to bridge this gap, a series of axial

66 compressive tests on CFST sections with WAAM steel elements has been conducted and is presented  
67 herein.

68 The process followed for the fabrication of the WAAM steel tubes is first presented, while the  
69 methods adopted for the determination of the as-built geometric properties of the examined specimens,  
70 featuring hand measurements, measurements based on Archimedes' principle and 3D laser scanning, are  
71 described. The results of complementary material tests, undertaken for the determination of the mechanical  
72 properties of the concrete and WAAM material, are then summarised. A description of the axial  
73 compressive tests on the CFST specimens is provided, while the test results are analysed and discussed.  
74 Finally, comparisons are made against the strength predictions yielded by current structural design  
75 specifications [18,52-57], and the results highlight the need to consider the influence of the weakening  
76 effect of the geometric undulations that are inherent to the WAAM process on the structural response of  
77 CFST sections.

## 78 **2. MANUFACTURE OF WAAM ELEMENTS**

79 Nine WAAM steel tubes of three different nominal thicknesses and diameters, and of two different lengths  
80 were manufactured for the compression tests, such that their nominal diameter to thickness ratios ranged  
81 from 30 to 100 and their nominal length to diameter ratios varied between 3.3 and 6.7. Oval steel tubes  
82 with flat sides and thicknesses of 3 mm and 6 mm were also manufactured, in order to obtain plates for  
83 the extraction of tensile coupons. The labels employed for the WAAM steel tubes include information  
84 regarding the diameter, thickness and length of the WAAM steel tube in mm. For example, Specimen  
85 D240T3L600 is a WAAM steel tube with a nominal diameter  $D_n$  of 240 mm, a nominal thickness  $t_n$  of 3  
86 mm and a nominal length  $L_n$  of 600 mm. For the tensile coupons, the identification system starts with the  
87 letter "H" or "V" for the coupons extracted horizontally or vertically relative to the deposition direction  
88 respectively, followed by the letter "A" or "M" for the coupons with their surface left in its as-built  
89 undulating state or machined smooth respectively, and, finally, by the test number. For example, Specimen  
90 H-A-1 is the first coupon with an as-built surface, extracted horizontally from within its parent plate, i.e.  
91 at a  $0^\circ$  angle to the deposition direction.

92 Printing of a subset of the WAAM circular hollow sections (CHS) and oval tubes is shown in Fig. 3.

93 The WAAM components were manufactured using a welding torch attached to a 6-axis robotic arm and a  
 94 metal inert gas (MIG) welding machine. The utilised shielding gas was a mixture of 97% Ar and 3% CO<sub>2</sub>.  
 95 The key parameters employed during the WAAM process are summarised in Table 1. The environmental  
 96 temperature and humidity of the room were 12 °C to 21 °C and 35% to 55%, respectively. The components  
 97 were printed layer-upon-layer, following the cross-section slice traces as defined in their digital models  
 98 created in Rhino 3D [58]. The feedstock material was carbon steel welding wire ER50-6, which was  
 99 deposited onto a Q235b steel substrate plate.

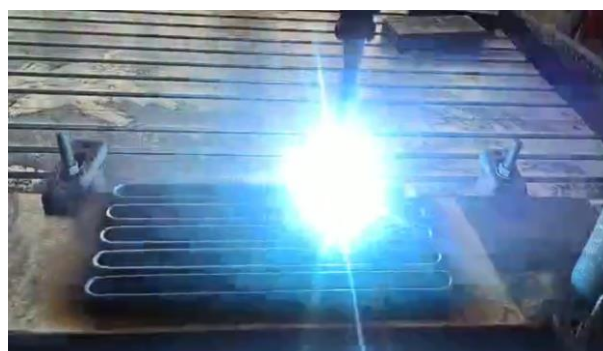
100 **Table 1** Process parameters used for WAAM specimens

Nominal thickness (mm)	Welding speed (m/min)	Wire feed rate (m/min)	Deposition rate (kg/h)	Wire feedstock diameter (mm)	Current (A)	Arc voltage (V)	Layer thickness (mm)
3	0.75	4	0.5-2	1.2	100-140	18-23	1.8
4	0.65-0.70	4	0.5-2	1.2	100-140	18-23	1.8
6	0.55-0.60	6.2-6.5	0.5-2	1.2	100-140	18-23	2.0

101 Following their fabrication, the WAAM CHS and oval tubes were detached from their substrate plates  
 102 using a plasma arc cutter. Note that a minimum distance equal to the outer diameter of the steel tube was  
 103 maintained between the base plate and the cutting line, to eliminate the influence of any initial printing  
 104 defects on the performance of the WAAM components. Both ends of the WAAM steel tubes were  
 105 machined to be flat and parallel and their exterior surfaces were sandblasted with glass beads to remove  
 106 any welding soot from the WAAM process.



(a) WAAM CHS for compression tests



(b) WAAM oval tubes with flat sides for tensile coupon tests

Figure 3. Printing of subset of WAAM CHS and oval tubes

107 **3. GEOMETRIC MEASUREMENTS**

108 The geometric characteristics of WAAM steel tubes are more variable than those of rolled sections due  
109 to the surface undulations arising from the printing process, rendering the use of conventional measuring  
110 techniques impractical. Thus, in order to obtain the as-built geometric properties of the WAAM steel  
111 tubes, three measuring methods were employed, featuring hand measurements, measurements based on  
112 Archimedes' principle and 3D laser scanning. The details of each method, as well as the obtained results,  
113 are discussed and compared in this section.

### 114 **3.1. Hand measurements**

115 A digital micrometre with an accuracy of 0.001 mm and a measuring tape were employed to provide  
116 baseline geometric data for the as-built WAAM components. For the WAAM steel tubes, the wall  
117 thickness  $t_h$  was determined as the average value of sixteen measurements taken at eight locations  
118 equally spaced around the section perimeter at both ends, utilising the digital micrometre - see Fig. 4(a).  
119 Similarly, measurements of the average perimeter  $C_h$  of the outer surface of each steel tube were taken  
120 at five locations evenly distributed along the member length, and their mean value was used to determine  
121 the average outer diameter  $D_h = C_h/\pi$ . Finally, the length  $L_h$  of each steel tube was determined based on  
122 four length measurements, taken at the locations indicated in Fig. 4(a). The average geometric properties  
123 of the steel tubes, as determined by the hand measurements, are listed in Table 2; the nominal thickness  
124  $t_n$ , nominal diameter  $D_n$  and nominal length  $L_n$  of each WAAM steel tube are also provided in Table 2.  $A_h$   
125 is the cross-sectional area and  $V_h$  is the volume calculated using the reported measured values. For the  
126 WAAM tensile coupons, the average width  $b_{C,h}$  and thickness  $t_{C,h}$  were determined based on hand  
127 measurements taken with the digital micrometre at eight locations evenly distributed along the parallel  
128 length of each coupon - see Fig. 4(b). The average values of  $b_{C,h}$  and  $t_{C,h}$ , along with the average cross-  
129 sectional area  $A_{C,h}$  of each coupon are listed in Table 3. The nominal widths and thickness of the  
130 coupons,  $b_{C,n}$  and  $t_{C,n}$ , respectively, are also provided in the table. In the present study, coupons with a  
131 nominal thickness of 6 mm were tested, while tests on corresponding 3 mm coupons have been reported  
132 in [15,59].

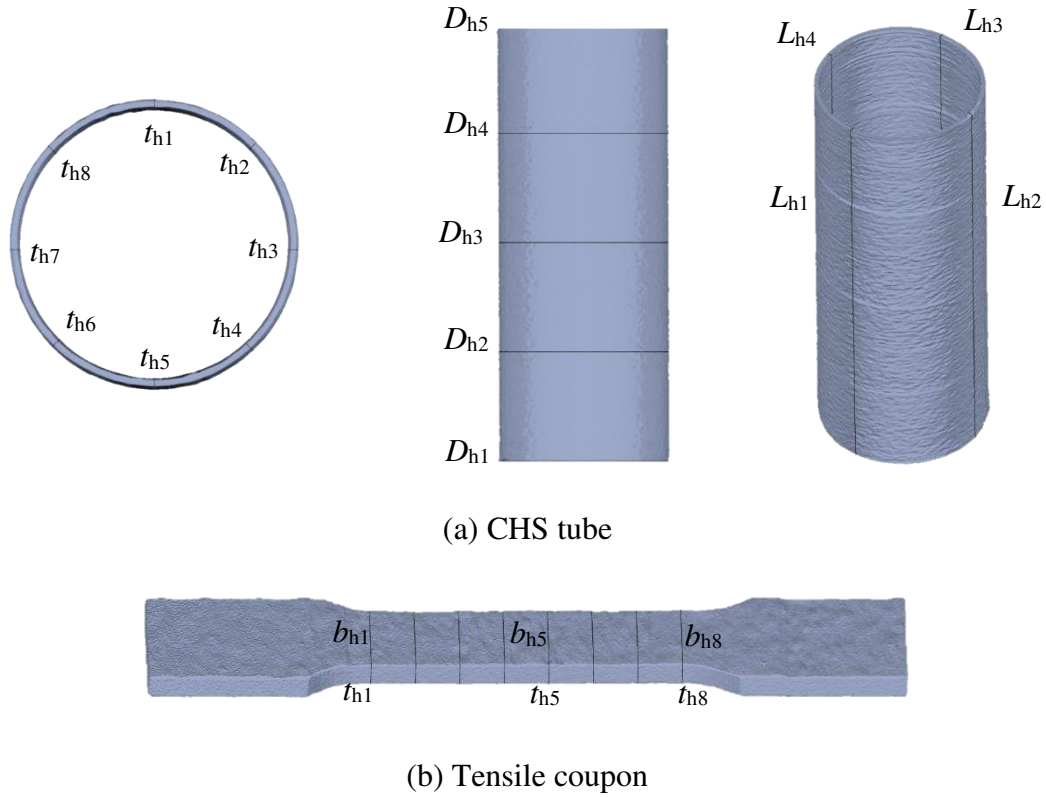


Figure 4. Locations of hand measurements for WAAM specimens

133 **3.2. Measurements based on Archimedes' principle**

134 Archimedes' principle, which is frequently employed for the determination of the porosity of concrete  
 135 elements [60,61], was employed herein for the calculation of the density of the WAAM material and  
 136 subsequently, the volume of the WAAM steel components. First, an electronic balance was used to  
 137 weigh the WAAM tensile coupons and tubes (with their masses labelled  $m_{C,Arch}$  and  $m_{Arch}$  respectively),  
 138 as shown in Fig. 5(a). A cylinder was then utilised to measure the volume of the tensile coupons  $V_{C,Arch}$   
 139 based on the water displacement method, as illustrated in Fig. 5(b), which allowed the determination of  
 140 the density  $\rho_{C,Arch}$  of each coupon, in line with Eq. (1).

141 
$$\rho_{C,Arch} = \frac{m_{C,Arch}}{V_{C,Arch}} \quad (1)$$

142 Finally, the average density  $\rho_{C,Arch}$  of all coupons, which was  $7903 \text{ kg/m}^3$ , was used for the  
 143 determination of the volume  $V_{Arch}$  of the steel tubes, based on their measured mass  $m_{Arch}$ . The measured  
 144 geometric properties of the WAAM steel tubes and steel coupons are reported in Tables 2 and 3,



145 respectively.



(a) Electronic balance

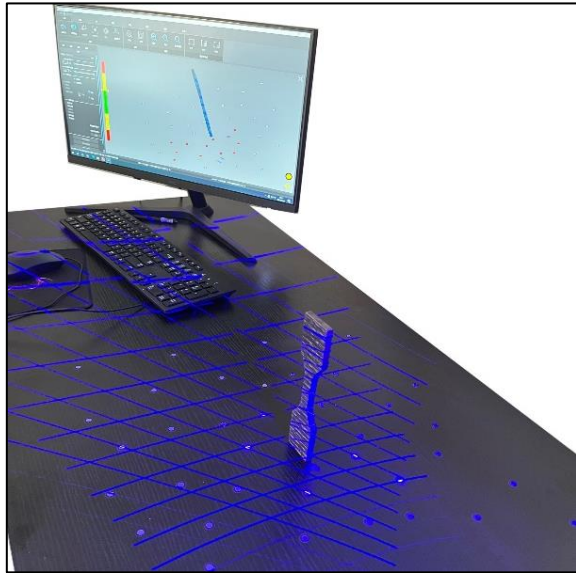


(b) Measuring cylinder

Figure 5. Equipment used for Archimedes' measurements

### 146 3.3. 3D laser scanning

147 3D laser scanning was employed to capture digitally the full geometry of the WAAM steel components  
148 prior to testing. A SCANTECH 3D laser scanner, capable of capturing up to 500,000 points per second  
149 with an accuracy of 0.05 mm, was employed to scan all the WAAM steel tubes and coupons. The  
150 acquired point cloud data were processed using the software Scanviewer. Following calibration of the  
151 scanner, markers were attached to the surfaces of the WAAM steel tubes and a flat plate on which the  
152 specimens were placed during scanning, to facilitate alignment of the relative coordinate systems of the  
153 3D point clouds during the coordinate conversion process. At least three markers need to be shared  
154 between adjacent scan views for merging to be realised.



(a) Typical coupon



(b) Typical steel tube

Figure 6. 3D laser scanning of WAAM specimens



(a) Coupon



(b) Steel tube

Figure 7. Comparisons of scanned surface profiles with respective specimens

155 The surface profiles of all steel coupons, as well as the outer surface profiles of the four steel tubes  
 156 (namely D240T3L600, D240T6L600, D300T3L600 and D300T6L600), were obtained with one  
 157 continuous scan, as shown in Fig. 6. Typical comparisons between scanned surface morphologies and  
 158 the respective WAAM components are shown in Fig. 7. The scanned 3D models (.stl) were subsequently  
 159 imported into the software Geomagic Wrap [62], for determination of their geometry. The volumes of  
 160 the WAAM steel tubes  $V_{Scan}$  and steel coupons  $V_{C,Scan}$ , as determined from the laser scans, are reported  
 161 in Tables 2 and 3, respectively.

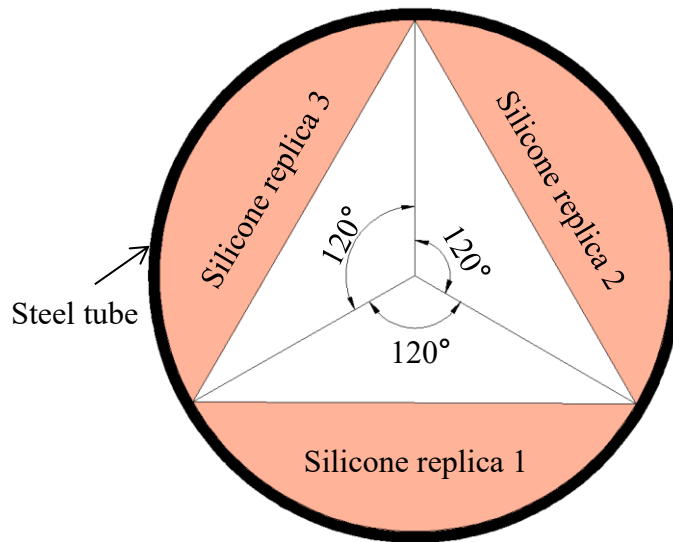


Figure 8. Illustration of silicone replicas of inner surface of tubes

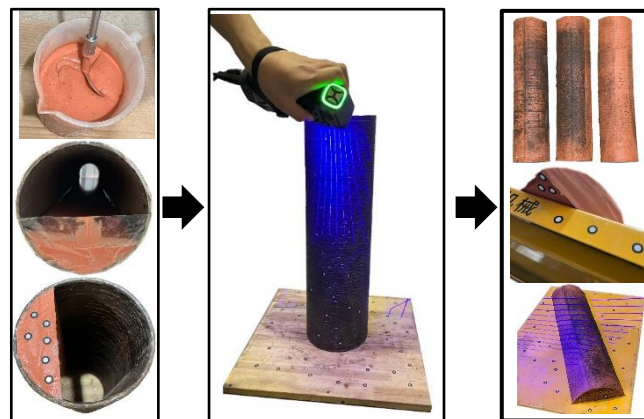
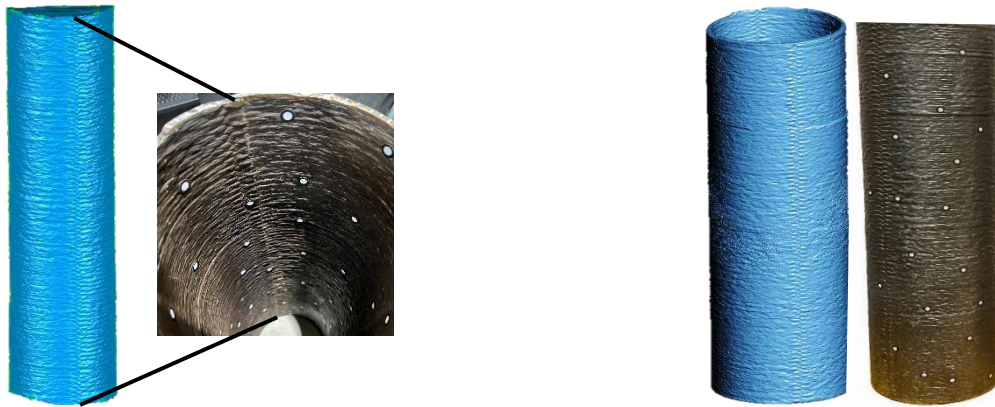


Figure 9. Production and scanning of silicone casts

162 The proportions of the WAAM steel tubes D180T3L600 and D180T6L600 were such that scanning  
 163 of the full inner surface profiles just from the two tube ends was not possible. Silicone casting was  
 164 therefore undertaken to form silicone replicas of the inner tube surface that could subsequently be  
 165 scanned [12]. In order to reduce the volume of silicone and facilitate removal of the silicone casts from  
 166 within the WAAM steel tubes, three moulds were created, as illustrated in Fig. 8, while silicone release  
 167 spray was applied to the inner tube surface. The prepared silicone mixture was slowly poured into the  
 168 tubes and allowed to set for at least 24 hours. Following setting, at least three markers were positioned  
 169 on each end of the silicone casts, as shown in Fig. 9, which were scanned together with the WAAM  
 170 tubes. The silicone casts were then removed from within the steel tubes and scanned individually. Finally,  
 171 the scans of the outer and inner tube surfaces were merged and converted into a complete 3D model. A  
 172 typical comparison between the scan of a silicone cast and the respective inner surface profile of a

173 WAAM steel tube is shown in Fig. 10(a), while a typical outer surface comparison is shown in Fig.  
174 10(b). Their geometric dimensions are summarised in Table 2.



(a) Inner surface of specimen D180T6L600

(b) Outer surface of specimen D180T6L600

Figure 10. Typical comparisons of scanned surface profiles

175 Capturing the inner surface geometries of the WAAM steel tubes D180T4L1200, D240T4L1200  
176 and D300T4L1200 was not practically possible even with silicone casting, due to their length. The  
177 average thicknesses and cross-sectional areas of these specimens were therefore determined based on  
178 the Archimedes' measurements.

**Table 2** Average measured geometric properties of WAAM steel tubes

Steel tube ID	$t_n$ (mm)	$D_n$ (mm)	$L_n$ (mm)	$t_h$ (mm)	$D_h$ (mm)	$L_h$ (mm)	$A_h$ (mm <sup>2</sup> )	$V_h$ (mm <sup>3</sup> )	$m_{Arch}$ (kg)	$V_{Arch}$ (mm <sup>3</sup> )	$V_{Scan}$ (mm <sup>3</sup> )	$\frac{V_h}{V_{Arch}}$	$\frac{V_{Scan}}{V_{Arch}}$
D180T3L600	3	180	600	2.91	179.68	617.4	1618.2	$999 \times 10^3$	8.05	$1019 \times 10^3$	$990 \times 10^3$	0.98	0.97
D240T3L600	3	240	600	3.10	238.94	611.3	2295.4	$1402 \times 10^3$	10.75	$1360 \times 10^3$	$1374 \times 10^3$	1.03	1.01
D300T3L600	3	300	600	3.13	299.87	614.9	2913.3	$1787 \times 10^3$	13.35	$1689 \times 10^3$	$1702 \times 10^3$	1.06	1.01
D180T6L600	6	180	600	6.58	179.54	611.1	3577.5	$2184 \times 10^3$	16.65	$2107 \times 10^3$	$2147 \times 10^3$	1.04	1.02
D240T6L600	6	240	600	6.46	239.66	608.3	4730.6	$2873 \times 10^3$	22.15	$2803 \times 10^3$	$2863 \times 10^3$	1.03	1.02
D300T6L600	6	300	600	6.54	298.97	609.6	6007.4	$3658 \times 10^3$	27.75	$3511 \times 10^3$	$3580 \times 10^3$	1.04	1.02
D180T4L1200	4	180	1200	3.69	179.63	1219.9	2039.6	$2482 \times 10^3$	19.10	$2417 \times 10^3$	-	1.03	-
D240T4L1200	4	240	1200	3.79	239.85	1219.4	2810.7	$3428 \times 10^3$	25.45	$3220 \times 10^3$	-	1.06	-
D300T4L1200	4	300	1200	3.82	299.95	1210.8	3553.8	$4292 \times 10^3$	31.75	$4018 \times 10^3$	-	1.07	-
											Mean	1.04	1.01
											CoV	0.026	0.018

**Table 3** Average measured geometric properties of WAAM steel coupons

Coupons		$b_{C,n}$	$t_{C,n}$	$b_{C,h}$	$t_{C,h}$	$A_{C,h}$	$m_{C,Arch}$	$V_{C,Arch}$	$V_{C,Scan}$	$\rho_{C,Arch}$	$\frac{V_{C,Scan}}{V_{C,Arch}}$
		(mm)	(mm)	(mm)	(mm)	(mm <sup>2</sup> )	(g)	(mm <sup>3</sup> )	(mm <sup>3</sup> )	(kg/m <sup>3</sup> )	
As-built steel	H-A-1	20	6	20.66	6.17	127.42	220.47	28000	27910	7873.9	1.00
	H-A-2	20	6	20.29	5.98	121.20	224.77	29000	28650	7750.7	0.99
	H-A-3	20	6	20.31	6.17	125.20	221.43	28500	28160	7769.5	0.99
	V-A-1	20	6	20.19	6.16	124.30	227.48	29000	28890	7844.1	1.00
	V-A-2	20	6	19.99	6.28	125.57	227.26	29000	28730	7836.6	0.99
	V-A-3	20	6	20.40	6.19	126.20	223.73	27500	27220	8135.6	0.99
Machined steel	H-M-1	20	6	20.47	5.31	108.67	196.09	25000	24570	7843.6	0.98
	H-M-2	20	6	20.32	5.11	103.96	185.30	23500	23070	7885.1	0.98
	V-M-1	20	6	20.24	5.37	108.73	195.98	24500	24280	7999.2	0.99
	V-M-2	20	6	20.05	4.78	95.99	169.90	21000	20980	8090.5	1.00
									Mean	7902.9	0.99
									CoV	0.016	0.006

183

**Table 4** Summary of average geometric properties and key test results of concrete-filled WAAM steel tubes, as determined by laser scanning

WAAM steel Tube ID	$t$ (mm)	$D$ (mm)	$L$ (mm)	$A$ (mm <sup>2</sup> )	$A_c$ (mm <sup>2</sup> )	$N_{u,Exp}$ (kN)	$\delta_{V,u}$ (mm)	$\delta_{H,u}$ (mm)	$DI$	$\frac{A}{A_{min}}$	$\frac{A}{A_{max}}$	$\frac{A_{sd}}{A}$
D180T3L600	2.89	178.08	617.2	1590.6	23316.3	1904	3.03	a	6.25	1.08	0.91	0.028
D240T3L600	3.00	237.94	610.9	2214.3	42251.4	3010	2.84	a	7.06	1.06	0.92	0.034
D300T3L600	3.06	295.23	614.5	2804.2	65651.7	4274	2.47	a	4.50	1.03	0.94	0.029
D180T6L600	6.44	178.46	615.6	3477.7	21535.7	2428	2.97	a	5.39	1.05	0.96	0.016
D240T6L600	6.40	238.19	608.1	4660.4	39898.7	3797	2.79	a	6.75	1.04	0.94	0.015
D300T6L600	6.47	297.90	609.3	5923.6	63776.1	5460	2.61	a	5.79	1.05	0.93	0.020
D180T4L1200	3.69 <sup>b</sup>	179.63 <sup>b</sup>	1219.9 <sup>b</sup>	2039.6 <sup>b</sup>	23302.8 <sup>b</sup>	2002	5.7	0.15	5.23			
D240T4L1200	3.79 <sup>b</sup>	239.85 <sup>b</sup>	1219.4 <sup>b</sup>	2810.7 <sup>b</sup>	42371.7 <sup>b</sup>	3208	5.46	0.61	5.39			
D300T4L1200	3.82 <sup>b</sup>	299.95 <sup>b</sup>	1210.8 <sup>b</sup>	3553.8 <sup>b</sup>	67108.5 <sup>b</sup>	4791	5.13	1.44	4.52			
									Mean	1.05	0.93	0.02
									CoV	0.019	0.017	0.328

184 Note: a signifies that for specimens with a length less than 1000 mm, their horizontal displacement was not measured; b signifies that the dimension of  
185 the WAAM steel tube was determined by the Archimedes' measurements.

186 **3.4. Comparison between measuring methods**

187 The measured volumes of the WAAM steel tubes determined using the different measuring methods are  
188 compared in Table 2. The volumes calculated using the hand measurements  $V_h$  differ somewhat from  
189 those obtained based on Archimedes' principle  $V_{Arch}$ , with their deviation ranging between -2% and 7%.  
190 On the contrary, the volumes  $V_{Scan}$  determined using the laser scans were very similar to those  
191 determined using Archimedes' principle  $V_{Arch}$ , with the mean value of  $V_{Scan}/V_{Arch}$  ratio being 1.01 and  
192 the coefficient of variation (CoV) being 0.018, providing confidence in the 3D laser scanning method.  
193 Similar conclusions were drawn for the geometric properties of the tensile coupons, as reported in Table  
194 3, with the mean value of  $V_{C,Scan}/V_{C,Arch}$  being 0.99 and the CoV being 0.006.

195 Overall, 3D laser scanning is deemed to be the most suitable method for determining accurate  
196 measurements of the geometry of the WAAM steel elements, while the hand and Archimedes'  
197 measurements served as reference values for comparison and verification purposes.

198 **3.5. Analysis of cross-sectional geometry of WAAM components**

199 The 3D models of the WAAM steel components obtained from the laser scans were imported into Rhino  
200 3D [65] for geometric analysis. Contouring of each component along its length was first undertaken, to  
201 accurately determine the cross-sectional dimensions. Processing of typical WAAM components in  
202 Rhino is shown in Fig. 11, where limited cross-sectional contours are presented for illustration purposes.

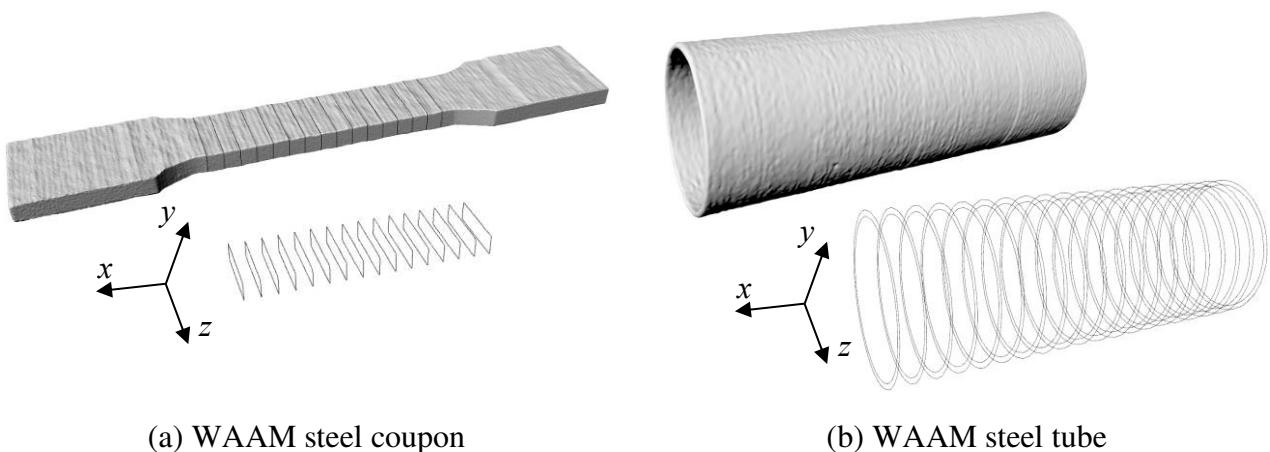


Figure 11. Scanned 3D model and cross-sectional contours of typical WAAM steel components



203 A sensitivity study was undertaken in order to determine the most suitable contour spacing for the  
 204 examined WAAM steel components. Two typical WAAM elements (i.e. the WAAM coupon H-A-1 and  
 205 the WAAM tube D180T6L600), were contoured at a spacing  $dx$  of 2.0 mm, 1.0 mm, 0.5 mm, 0.2 mm  
 206 and 0.1 mm and their cross-sectional areas were subsequently determined. The obtained results are  
 207 shown in Fig. 12, in which the mean, minimum and maximum values of the cross-sectional areas ( $A$ ,  
 208  $A_{\min}$  and  $A_{\max}$ ) determined from the different contour spacings are normalised by the corresponding  
 209 values determined using a contour spacing  $dx = 0.1$  mm. As expected, the values of  $A_{\min}$  and  $A_{\max}$  were  
 210 more sensitive to the contour spacing compared to the mean value of  $A$ . Since it was found that the  
 211 cross-sectional areas obtained using a contour spacing  $dx = 0.2$  mm were almost equal to those obtained  
 212 with a contour spacing  $dx = 0.1$  mm, a value of  $dx = 0.2$  mm was adopted for the conducted geometric  
 213 analyses. It should be noted that the adopted spacing of 0.2 mm was about 10% of the WAAM layer  
 214 height, which was equal to approximately 2.0 mm, as shown in Fig. 13.

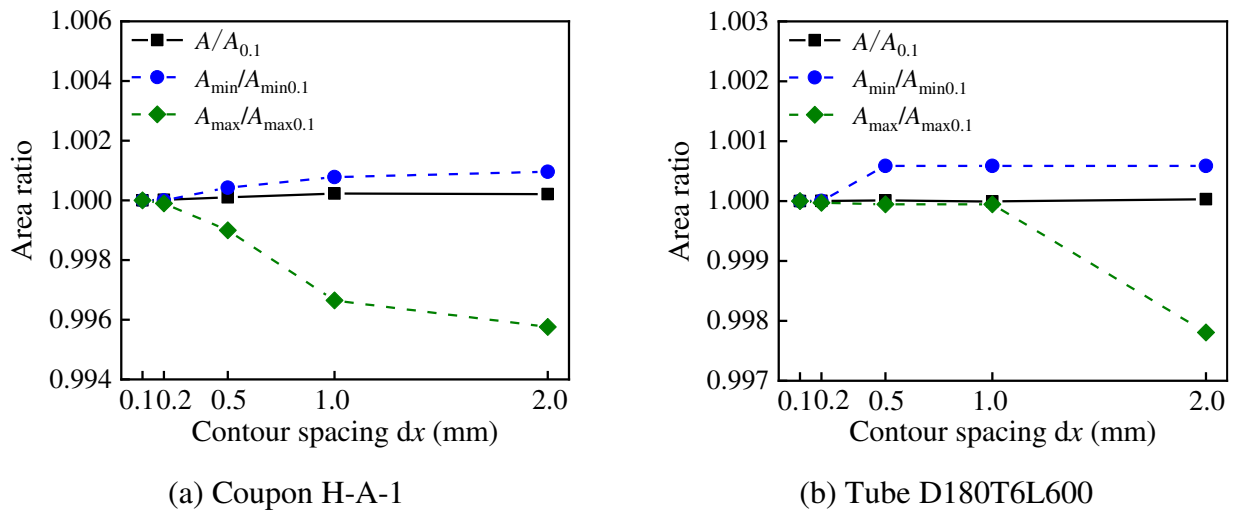


Figure 12. Sensitivity of cross-sectional area measurements to variation in contour spacing  $dx$

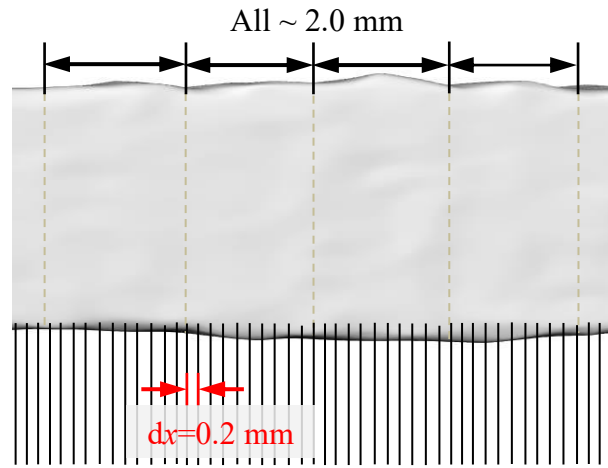


Figure 13. WAAM layer height ( $\sim 2.0$  mm) and adopted contour spacing  $dx$  of 0.2 mm

215 A summary of the geometric properties of the WAAM steel elements is reported in Tables 4 and 5,  
 216 where  $t$ ,  $D$  and  $L$  are the mean values of the wall thickness, outer diameter and length of the WAAM  
 217 steel tubes, respectively, and  $A$ ,  $A_{\min}$  and  $A_{\max}$  are the mean, minimum, and maximum values of the  
 218 cross-sectional areas. Comparisons between the mean, minimum and maximum values through the ratio  
 219  $A/A_{\min}$  and  $A/A_{\max}$  are also presented in Tables 4 and 5. Reasonable differences (up to 4%) were  
 220 observed between the  $A$ ,  $A_{\min}$  and  $A_{\max}$  values of the same WAAM member, which are attributed to  
 221 the undulations of the WAAM surface.

222 **Table 5** Summary of the geometric properties of the WAAM steel coupons as determined by the laser  
 223 scanning

WAAM steel coupon ID	$A$ (mm <sup>2</sup> )	$A_{\min}$ (mm <sup>2</sup> )	$A_{\max}$ (mm <sup>2</sup> )	$\frac{A}{A_{\min}}$	$\frac{A}{A_{\max}}$	$\frac{A_{sd}}{A}$
H-A-1	123.67	119.62	128.52	1.03	0.96	0.014
H-A-2	124.46	123.24	127.04	1.01	0.98	0.014
H-A-3	123.22	122.56	126.25	1.01	0.98	0.013
H-M-1	108.67	107.44	110.21	1.01	0.99	0.012
H-M-2	103.96	101.74	105.22	1.02	0.99	0.012
V-A-1	124.52	119.57	129.11	1.04	0.96	0.018
V-A-2	124.86	120.23	129.09	1.04	0.97	0.016
V-A-3	124.84	119.81	129.29	1.04	0.97	0.017
V-M-1	108.73	106.49	109.73	1.02	0.99	0.011
V-M-2	95.99	93.15	97.09	1.03	0.99	0.010
			Mean	1.03	0.98	0.014
			CoV	0.013	0.012	-

224 The variation in the cross-sectional area for typical WAAM steel components (i.e. coupons V-A-1  
 225 and H-A-1 and tubes D180T6L600 and D240T3L600) is shown in the histograms in Fig. 13, where each

226 cross-sectional area measurement  $A_i$  is normalised by the average cross-sectional area  $A$  of the  
 227 corresponding WAAM specimen. The CoV values of the cross-sectional area, defined as the ratio of the  
 228 standard deviation of the area to the average area i.e.  $A_{sd}/A$  of each component, are reported in Tables 4  
 229 and 5. It can be seen that the values of  $A_{sd}/A$  range between 0.010 and 0.034, with the degree of dispersion  
 230 decreasing with increasing thickness of the WAAM steel, as also reported by Kyvelou et al. [12].

231 The geometric dimensions of the WAAM steel tubes, determined as described above, were used  
 232 for the subsequent analysis of the CFST specimens reported hereinafter. Exceptions to this are the larger  
 233 (1200 mm) specimens, for which full laser scanning was not possible and thus the Archimedes'  
 234 measurements were used – see Table 4, in which  $A_c$  is the mean cross-sectional area of the inner  
 235 concrete, where the geometric dimensions, as well as the key test results, are provided.

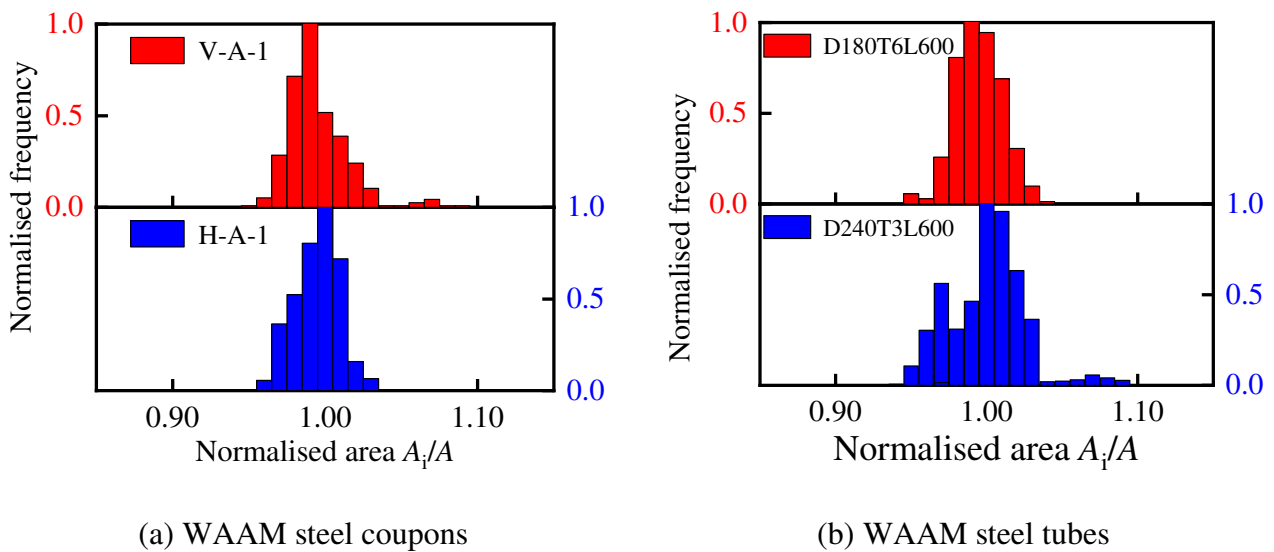


Figure 13. Distribution of normalised areas  $A_i/A$  of typical WAAM coupons and tubes

## 236 4. MATERIAL TESTS

### 237 4.1. Monotonic tensile tests

238 The material properties of the WAAM steel coupons, as well as their overall stress-strain response, were  
 239 determined in compliance with GB/T 228.1-2010 [63]. The tensile coupons were extracted from the  
 240 WAAM ovals at  $0^\circ$  and  $90^\circ$  to the deposition direction, as illustrated in Fig. 14, to assess the material  
 241 anisotropy. Coupons of two different nominal thicknesses (i.e. 3 mm and 6 mm) were tested, while the

242 effect of the geometric undulations on the material properties was also investigated by comparing the  
 243 response of as-built and machined coupons. In total, 20 tensile tests were conducted.

244 For the machined coupons, an electrical resistance strain gauge was attached at the mid-height on  
 245 one side of each coupon to record longitudinal strains during the early stages of testing while, for both  
 246 the machined and as-built coupons, an extensometer and a digital image correlation (DIC) system were  
 247 employed to provide detailed measurements of the surface strain field throughout testing. Prior to testing,  
 248 the parallel length of all coupons was painted white and then spray-painted with a random black speckle  
 249 pattern, in order for the strains to be calculated over the full area of the parallel length. A 250 kN  
 250 INSTRON testing machine operating in displacement control at a rate of 0.8 mm/min, was employed to  
 251 apply the tensile load. The load, strain gauge and extensometer measurements were recorded at a  
 252 frequency of 1 Hz, while the DIC system recorded the tensile force through an analogue to digital  
 253 converter and the images at a frequency of 1 Hz.

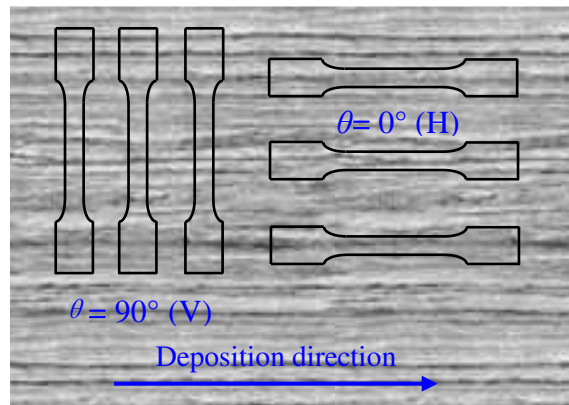


Figure 14. Orientation of tensile coupons extracted from WAAM plate relative to deposition direction

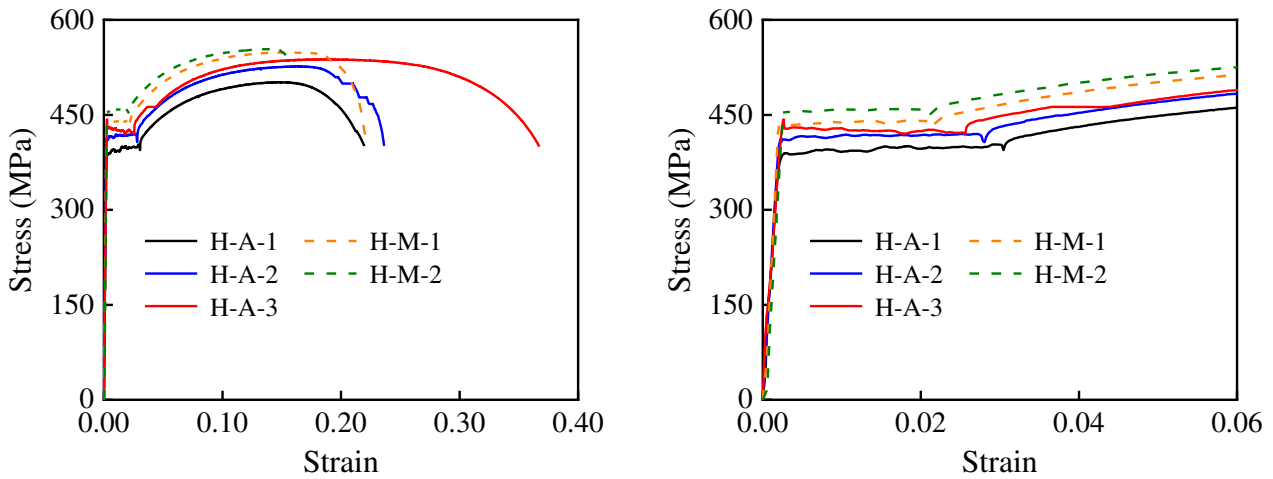
254

**Table 6** Average material properties of WAAM steel coupons

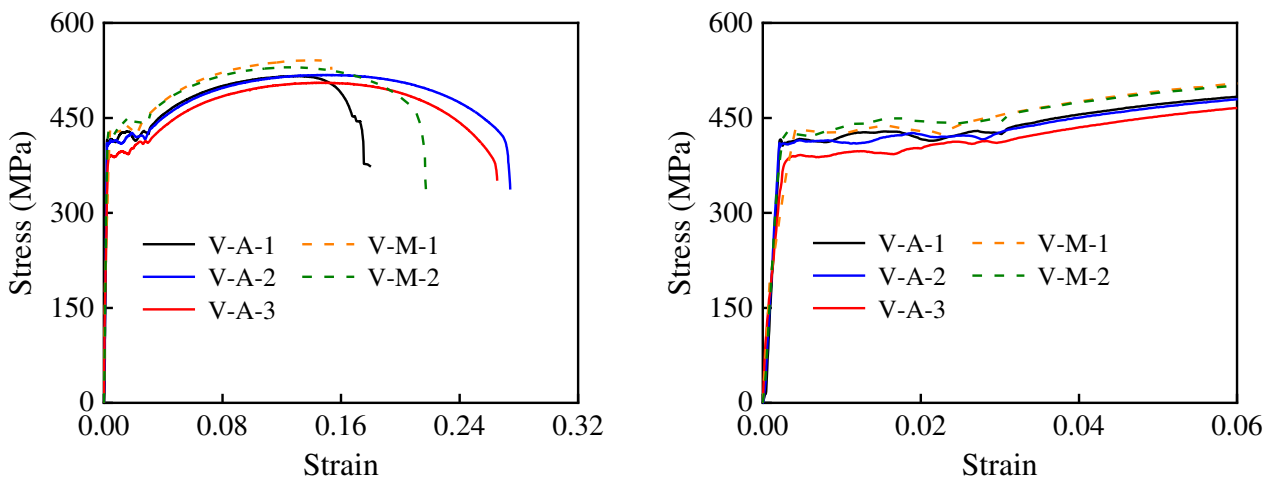
$\theta$	$t_{C,n}$ (mm)	$E$ (GPa)	$f_y$ (MPa)	$f_u$ (MPa)	$\epsilon_f$	Surface
$90^\circ$	6	205	405	513	0.20	As-built
		199	420	535	0.17	Machined
	3 <sup>[15,59]</sup>	198	408	515	0.09	As-built
$0^\circ$	6	209	411	522	0.24	As-built
		199	445	551	0.18	Machined
	3 <sup>[15,59]</sup>	186	478	563	0.15	As-built

255 The obtained stress-strain curves for the 6 mm coupons are shown in Fig. 15, while a summary of  
 256 the average material properties of the as-built and machined coupons, grouped by deposition direction

257 (i.e.  $0^\circ$ , and  $90^\circ$ ), is reported in Table 6, where  $E$  is the Young's modulus,  $f_y$  is the yield strength,  $f_u$  is  
 258 the ultimate tensile strength and  $\varepsilon_f$  is the fracture strain measured over the standard gauge length. Overall,  
 259 the mechanical properties of the as-built coupons were found to be somewhat lower than those of the  
 260 machined coupons, reflecting the negative influence of the WAAM surface undulations. Finally, mild  
 261 anisotropy was observed, which was found to be more pronounced for the thinner coupons.



(a) Tensile coupons at  $0^\circ$  (H) to the deposition direction



(b) Tensile coupons at  $90^\circ$  (V) to the deposition direction

Figure 15. Stress-strain curves obtained from tensile tests on 6 mm coupons: full curve (left), initial range (right)

#### 262 4.2. Concrete cube tests

263 Four concrete cubes were tested according to GB/T 50081-2002 [64] to obtain the material properties  
 264 of the inner concrete. All tests were completed soon after the completion of the 28-day curing period.  
 265 Based on the obtained test results, the mean compressive strength of the concrete was found to be  
 266  $f_{cu} = 41.33$  MPa. Thus, the cylinder compressive strength of the inner concrete, which was used to

267 calculate the axial compressive strength of the concrete filled WAAM steel tube specimens, was taken  
 268 as  $f_c = 0.8f_{cu} = 33.06$  MPa [65], while the elastic modulus was taken as  $E_c = 4730\sqrt{f_c} = 27200$  MPa  
 269 [55].

## 270 5. AXIAL COMPRESSION TESTS ON CFST SPECIMENS

### 271 5.1. Specimen preparation and test setup

272 Following mixing, the concrete was cast into the WAAM steel tubes, and was allowed to cure for 28  
 273 days. An end plate was welded to each end of the specimens to facilitate the application of the  
 274 compressive force during testing and to ensure its even distribution. Nine CFST specimens were tested  
 275 in total to investigate their mechanical behaviour under axial compression. The experimental layout  
 276 adopted for the conducted tests is shown in Fig. 16. A 10,000 kN electric-hydraulic jack was used for  
 277 the application of the axial load, operating at a constant displacement rate of 1 mm/min. Spherical hinge  
 278 supports were employed at the specimen ends, with the distance between them considered as the  
 279 effective length  $L_0$  of the specimens - see Fig. 16. This setup has been successfully used in the past for  
 280 CHS stub column tests [66,67]. Note that the geometric centroids of the ends of the specimens were  
 281 aligned with the centroid of the spherical bearing to avoid eccentricity of loading.

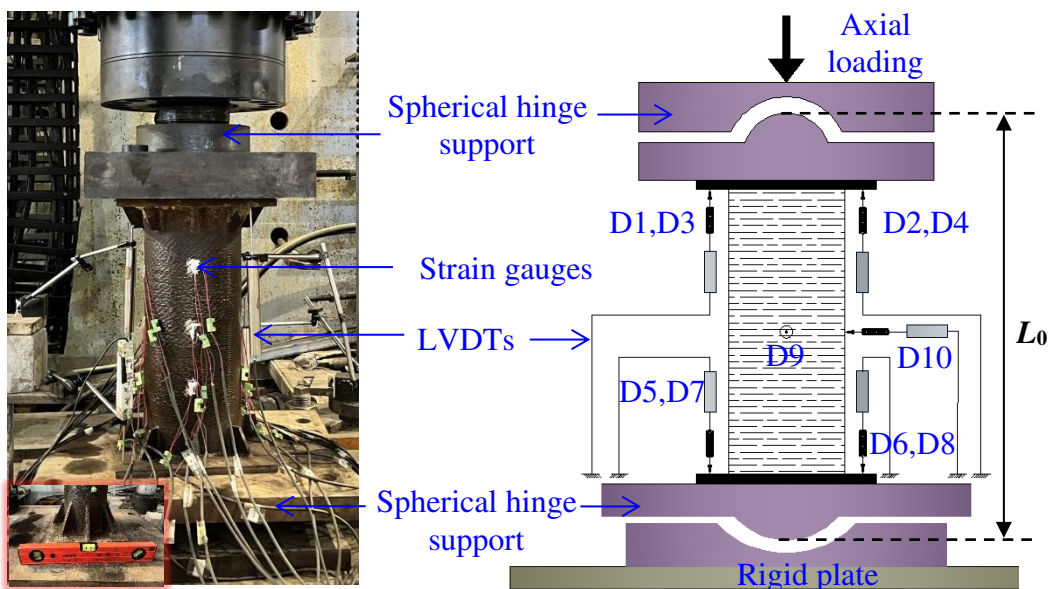


Figure 16. Test setup for axial compression tests on CFST specimens

### 282 5.2. Instrumentation

283 For the CFST specimens with a length of less than 1000 mm, eight LVDTs (D1-D8) were  
 284 symmetrically positioned at both specimen ends to measure the vertical displacements (D1-D4 at the  
 285 top end and D5-D8 at the bottom end), while, for the CFST specimens with a length of more than 1000  
 286 mm, two additional LVDTs (D9 and D10) were used to measure the lateral displacements, as shown in  
 287 Fig. 16. Twelve transverse and twelve longitudinal strain gauges ( $S_{T1}$ - $S_{T12}$  and  $S_{L1}$ - $S_{L12}$ ) were attached  
 288 to the CFST specimens at mid-height and the two 1/4-heights, as shown in Fig. 17, to measure the  
 289 vertical and horizontal hoop strains. Prior to attaching the strain gauges, the surface of the WAAM steel  
 290 tubes was locally sanded and polished to provide a smooth surface for adhesion. During testing, the load  
 291 was stopped when the displacement of the load cell reached 80 mm. The load cell, LVDT and strain  
 292 gauge readings were taken at a frequency of 1 HZ, using the DH3817 static data acquisition system.

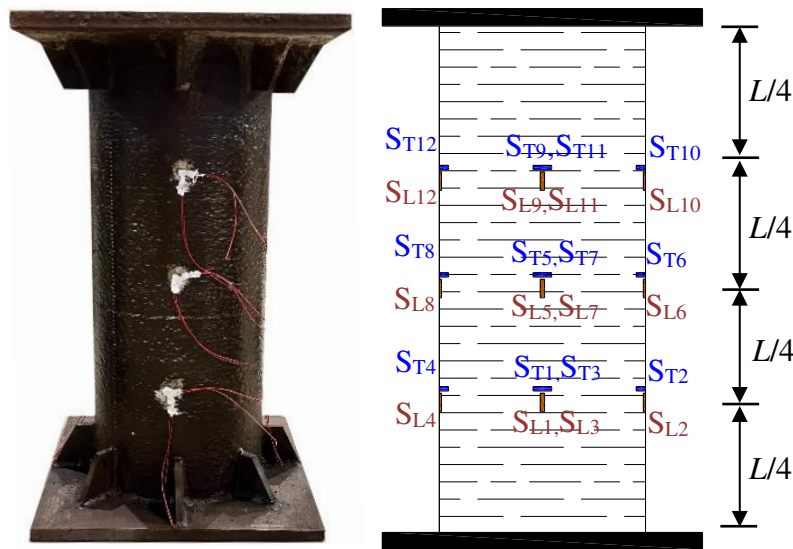


Figure 17. Arrangement of strain gauges on CFST specimens

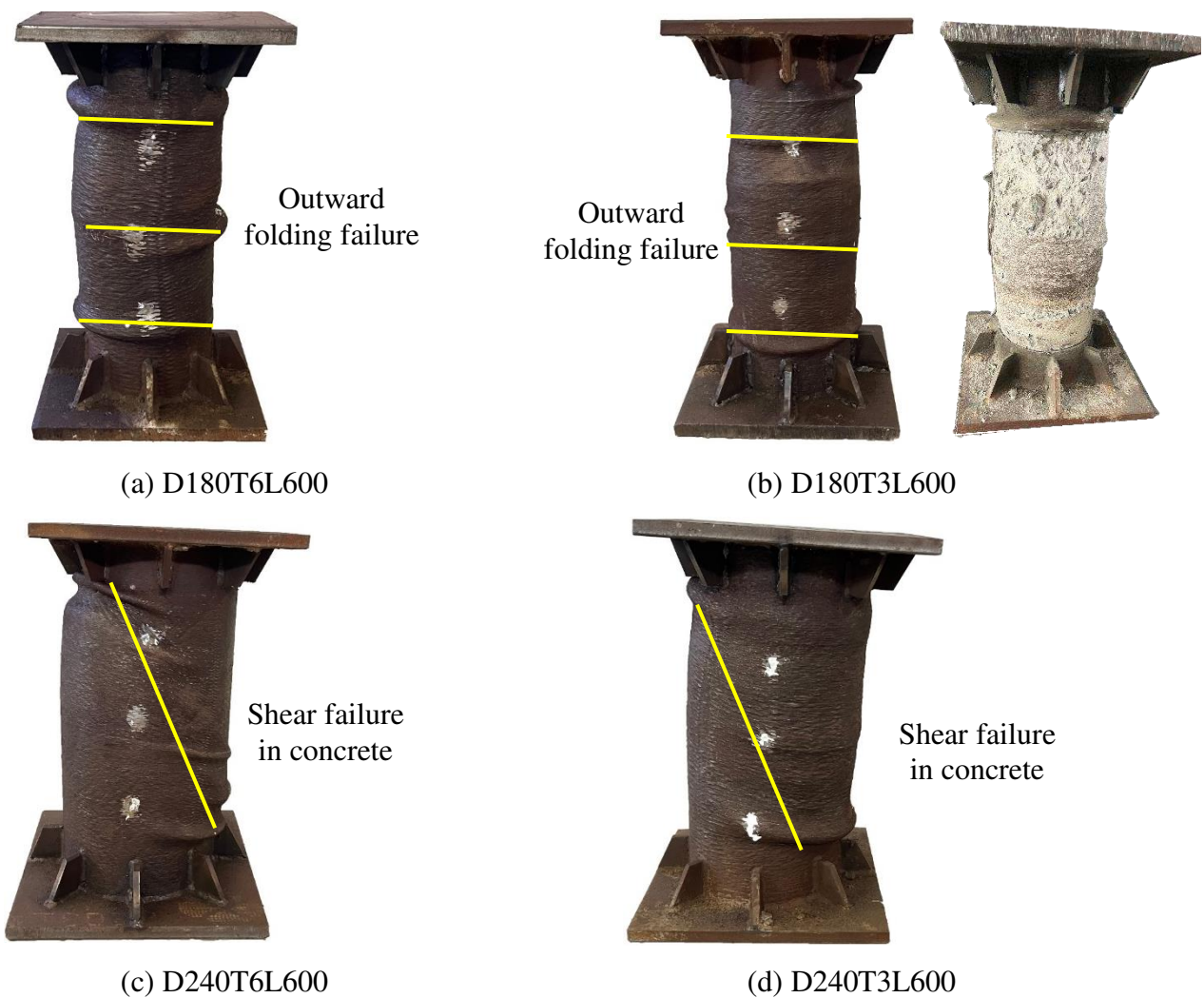
### 293 5.3. Results and discussion

#### 294 5.3.1. Failure modes and ultimate capacities

295 The failure modes of the CFST specimens are presented in Fig. 18. The failure modes of all CFST  
 296 specimens involved inelastic local buckling of the WAAM steel tubes and concrete crushing. More  
 297 specifically, CFST specimens D180T6L600 and D180T3L600 failed due to outward folding of the  
 298 section, as shown in Figs. 18(a) and (b), while for the rest of the CFST specimens, shear failure of the  
 299 inner concrete occurred, as shown in Figs. 18(c)-(i). The observed failure modes were generally similar



300 to those described by other researchers [41,47,68-71] for CFST members with conventionally produced  
301 straight seam steel tubes. It should also be mentioned that, unlike for CFST members fabricated from  
302 conventional steel tubes, where fracture of the steel tubes is often observed, no fracture occurred for the  
303 specimens examined herein. This is attributed to the WAAM tubes being composed of continuously  
304 printed 'hoop' of high ductility that were able to effectively resist the outward pressure from the confined  
305 concrete, in contrast to the seam welds running along the length of traditionally fabricated tubes that act  
306 as weak points. The continuous 'hoop' and the resulting absence of fracture had a positive impact on  
307 the ductility of the specimens after the attainment of their ultimate load.







(e) D300T6L600



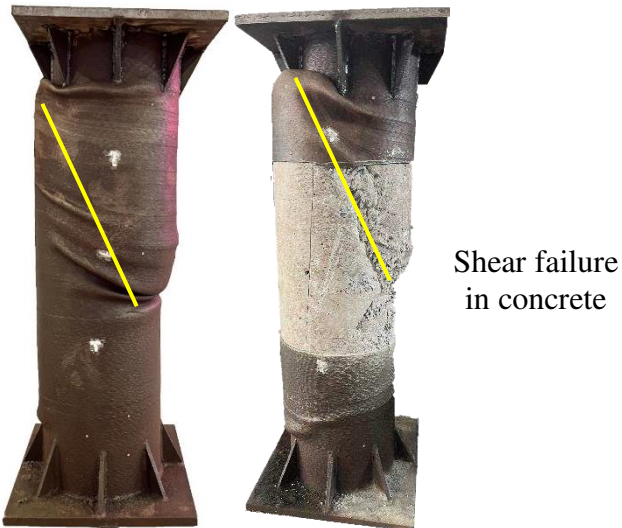
(f) D300T3L600



(g) D300T4L1200



(h) D240T4L1200



(i) D180T4L1200

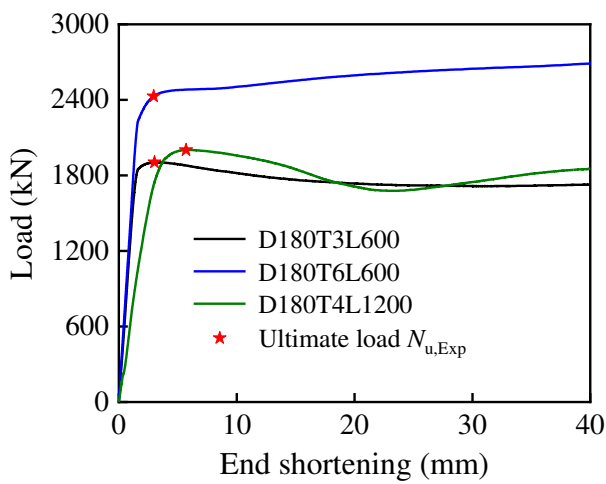
Figure 18. Failure modes of CFST specimens

308 The ultimate loads  $N_{u,Exp}$  of the CFST specimens, as well as the corresponding vertical  $\delta_{V,u}$  and  
309 horizontal displacements  $\delta_{H,u}$  obtained in the experiments are summarised in Table 4. As expected, the

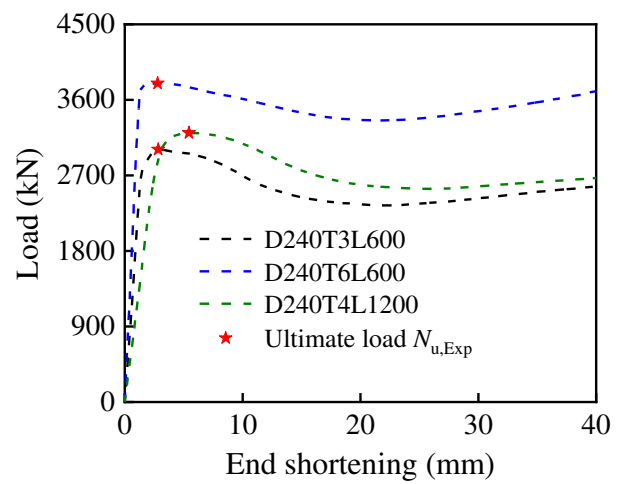
310 cross-sectional area had the most marked influence on the load-carrying capacity, with the ultimate load  
 311  $N_{u,Exp}$  increasing with increasing of cross-sectional area. Note that the lateral displacement at ultimate  
 312 load, which were only measured for the longer specimens (D180T4L1200, D240T4L1200 and  
 313 D300T4L1200), were significantly lower than the corresponding axial shortening - see Table 4,  
 314 indicating a minimal influence of global instability in the CFST experiments.

### 315 5.3.2. Load-end shortening curves

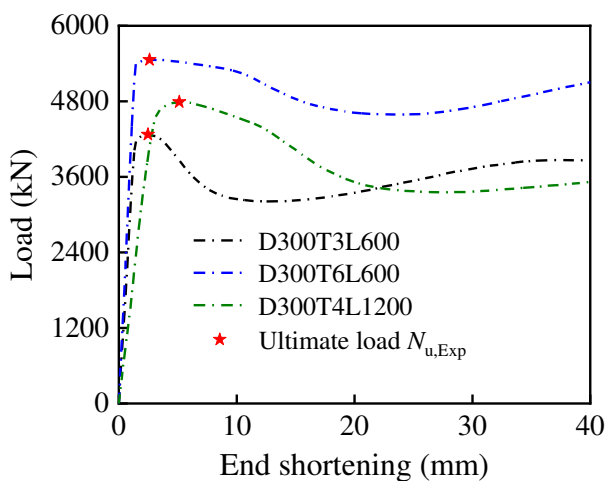
316 The load-end shortening curves of all CFST specimens obtained from the axial compression tests are  
 317 illustrated in Fig. 19. The specimens exhibited a linear elastic response in the early stages of loading.  
 318 This was followed by yielding of the WAAM tube, characterised by a sharp drop in stiffness but with  
 319 no visible outward deformations. Finally, development of significant local buckling of the WAAM steel  
 320 tube and crushing of the inner concrete led to the attainment of the ultimate load of the specimens.



(a) D180 series

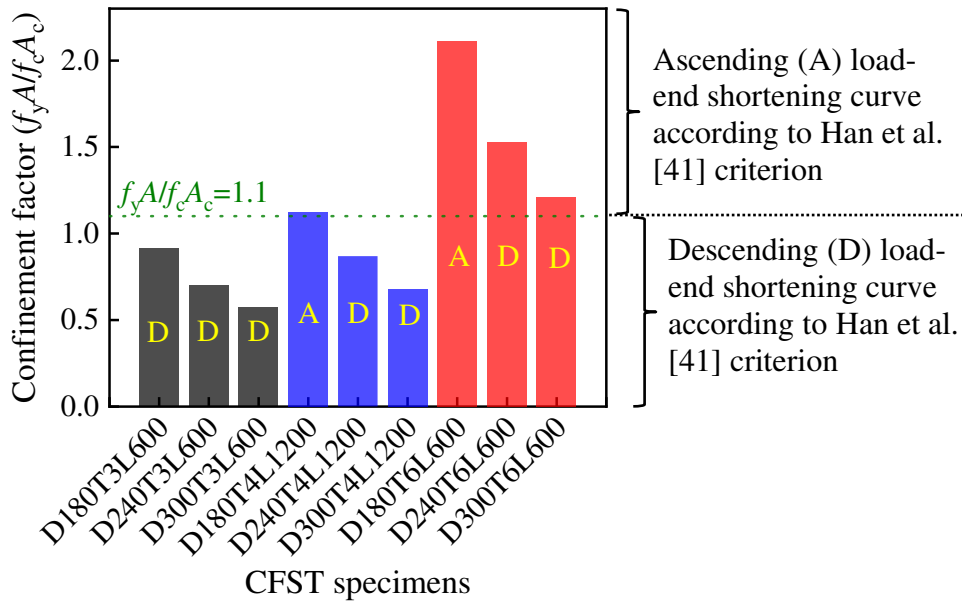


(b) D240 series

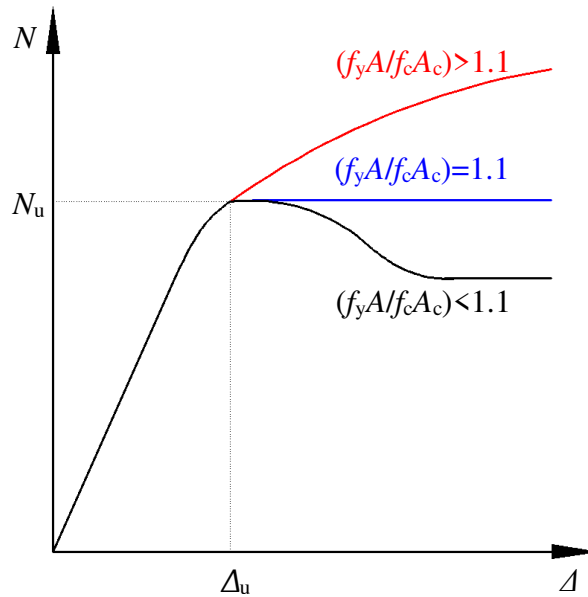


(c) D300 series

Figure 19. Load-end shortening curves of CFST specimens



(a) Confinement factors ( $f_y A / f_c A_c$ )



(b) Typical load-deformation ( $N-\Delta$ ) characteristics (Han et al. [41])

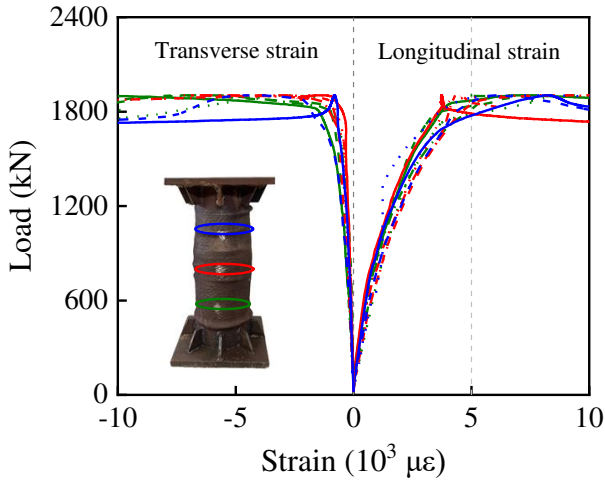
Figure 20. Comparison of confinement factors and load-deformation characteristics of CFST specimens

321 According to Han et al. [41], for conventional CFST members with diameter-to-thickness ratios  
 322 within the examined range (i.e. 30-134), the profile of the load-end shortening curve is related to the  
 323 confinement factor  $f_y A / f_c A_c$ , where  $f_y$  and  $A$  are the yield strength and cross-sectional area of the  
 324 WAAM steel tube and  $f_c$  and  $A_c$  are the cylinder compressive strength and cross-sectional area of the  
 325 inner concrete. The confinement factors of the specimens examined herein are presented in Fig. 20. A

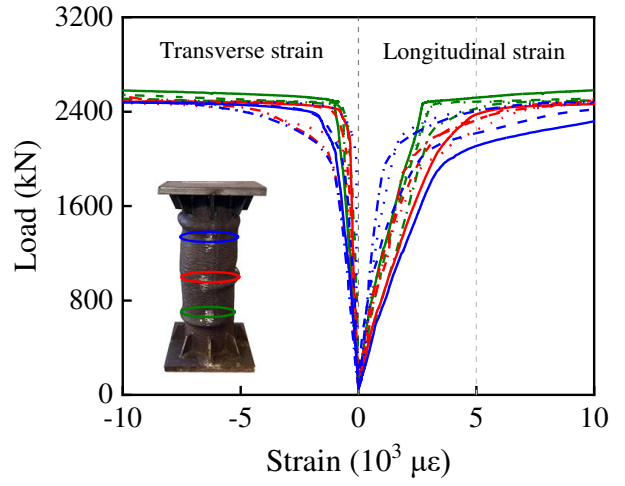
326 confinement factor greater than 1.1 corresponds to a continuously ascending load-end shortening curve  
327 with increasing load, while a confinement factor less than 1.1 corresponds to a load-end shortening curve  
328 that decreases after attainment of the peak load, according to the observations of Han et al. [41].  
329 Otherwise, when  $f_y A / f_c A_c \approx 1.1$ , a plateau in the load-end shortening curve after failure is anticipated  
330 [41]. It can be seen from Figs. 19 and 20 that, except for Specimens D240T6L600 and D300T6L600,  
331 the load-end shortening curves of all specimens follow the anticipated trends, as described by Han et al.  
332 [41]. The post-peak performance of Specimens D240T6L600 and D300T6L600 may have been  
333 influenced more than others by surface undulations in the steel tube that are inherent to the WAAM  
334 process.

### 335 5.3.3. Load-strain curves

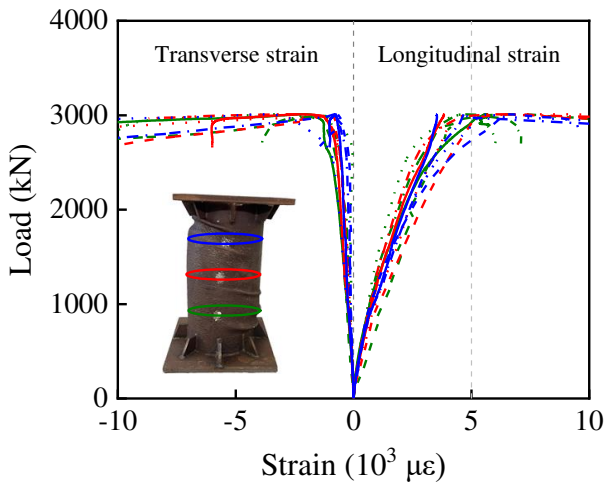
336 The load versus longitudinal and transverse strains experienced by the CFST test specimens at three  
337 locations along the member length are plotted in Fig. 21. The longitudinal and transverse strains were  
338 measured by the strain gauges labelled  $S_{L1}$ -  $S_{L12}$  and  $S_{T1}$ -  $S_{T12}$ , respectively – see Fig. 17, with positive  
339 values indicating compression and negative values indicating tension. Note that the load–transverse  
340 strain curves were employed to monitor the confinement of the concrete provided by the WAAM steel  
341 tubes. The different colours of the curves in Fig. 21 represent the strains at the three different locations  
342 along the specimen length. Lines of the same colour but different type represent the strains at different  
343 circumferential positions at the same height. It can be seen that there is somewhat of a spread in  
344 longitudinal strain readings in the early stages of loading; this is attributed to some inevitable non-  
345 uniformity in loading and properties of the infill concrete, as well as the influence of the surface  
346 undulations of the WAAM tubes. After the attainment of the peak load, the spread in longitudinal strain  
347 readings increases further, heralding the occurrence of local buckling.



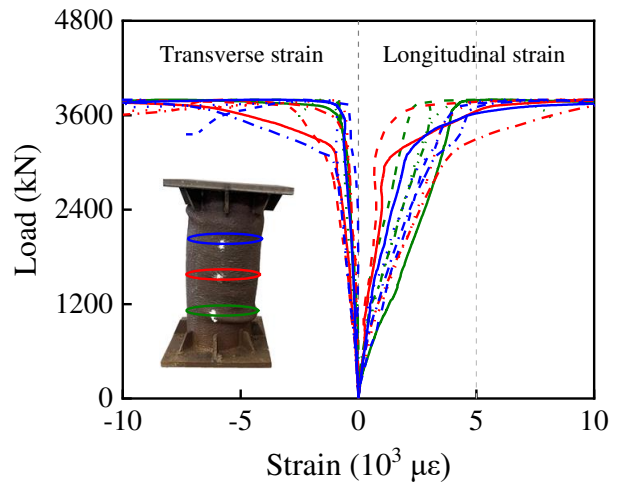
(a) D180T3L600



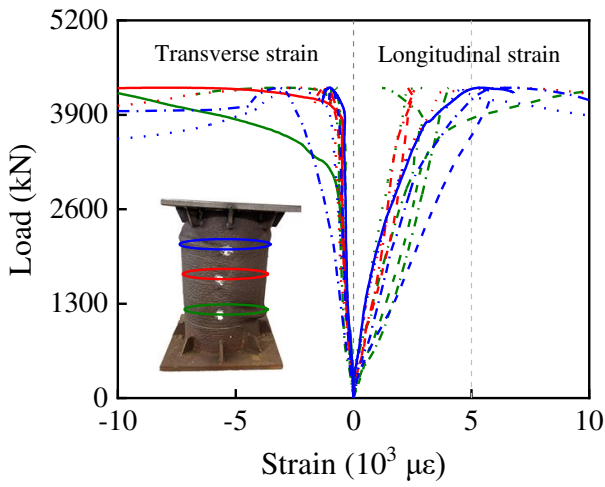
(b) D180T6L600



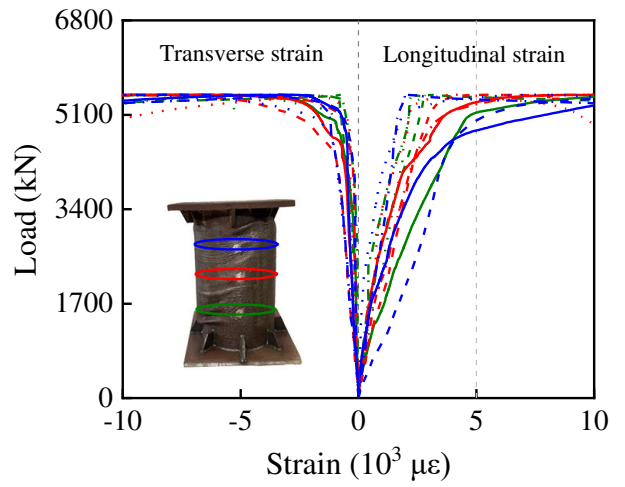
(c) D240T3L600



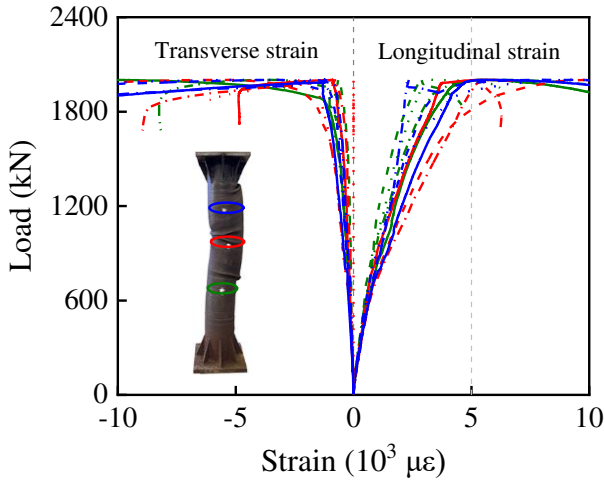
(d) D240T6L600



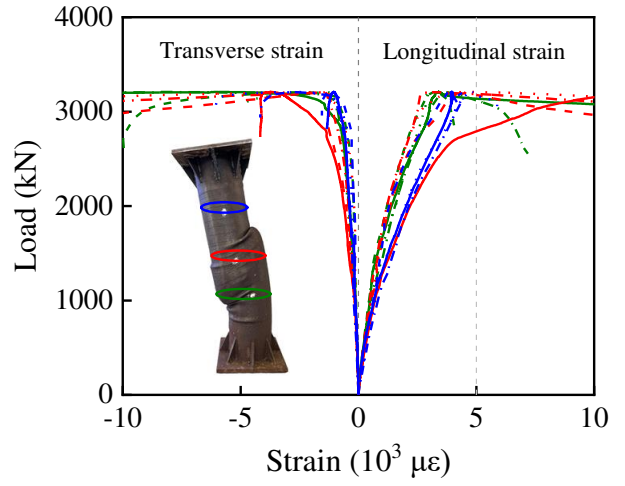
(e) D300T3L600



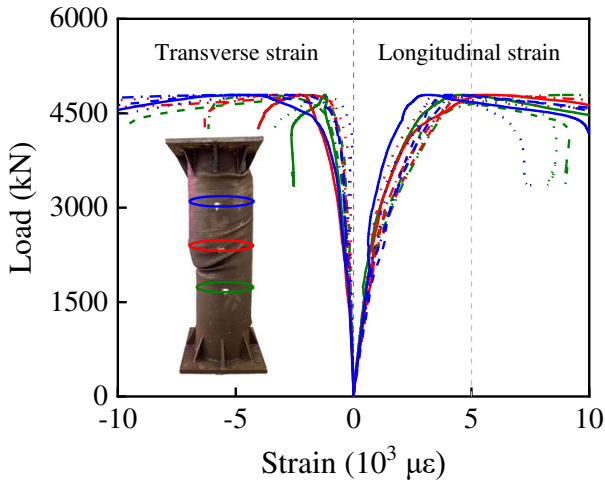
(f) D300T6L600



(g) D180T4L1200



(h) D240T4L1200



(i) D300T4L1200

Figure 21. Load–strain curves of CFST specimens

348 5.3.4. Ductility

349 To investigate the ductility of the CFST specimens, the ductility index  $DI$  [41,72] given by Equation (2)  
 350 was adopted.

351 
$$DI = \frac{\varepsilon_{0.85}}{\varepsilon_b} \quad (2)$$

352 In Equation (2),  $\varepsilon_{0.85}$  is the axial strain in the specimen when the load falls to 85% of the ultimate load  
 353 (see Fig. 22(a)) and  $\varepsilon_b$  is equal to  $\varepsilon_{0.75} / 0.75$ , in which  $\varepsilon_{0.75}$  is the axial strain in the specimen when the  
 354 load attains 75% of the axial compressive strength in the pre-ultimate stage, as shown in Fig. 22(a). It  
 355 should be noted that for the specimens without a 15% decrease in ultimate load after the attainment of

356 the axial compressive strength,  $\varepsilon_{0.85}$  was taken as three times the strain at their ultimate load ( $3\varepsilon_u$ ) for  
 357 the calculation of  $DI$  [73].

358 The ductility indices  $DI$  calculated using Eq. (2) for all WAAM CFST specimens are shown in  
 359 Table 4. The  $DI$  values are also plotted in Fig. 22(b) against the tube diameter to wall thickness ratio  
 360  $D/T$ , and compared with corresponding  $DI$  values determined from tests on a sample of CFST members  
 361 comprising conventional steel tubes [41]. The results show that the range of calculated  $DI$  values for the  
 362 WAAM CFST specimens varied from 4.5 to 7.1, and were consistently higher than the  $DI$  values for the  
 363 corresponding conventional CFST members; this is attributed to the high ductility of the WAAM steel  
 364 tube and the fact that higher grade and less ductile concrete (C80) was used in the conventional  
 365 specimens against with which the present specimens are compared.

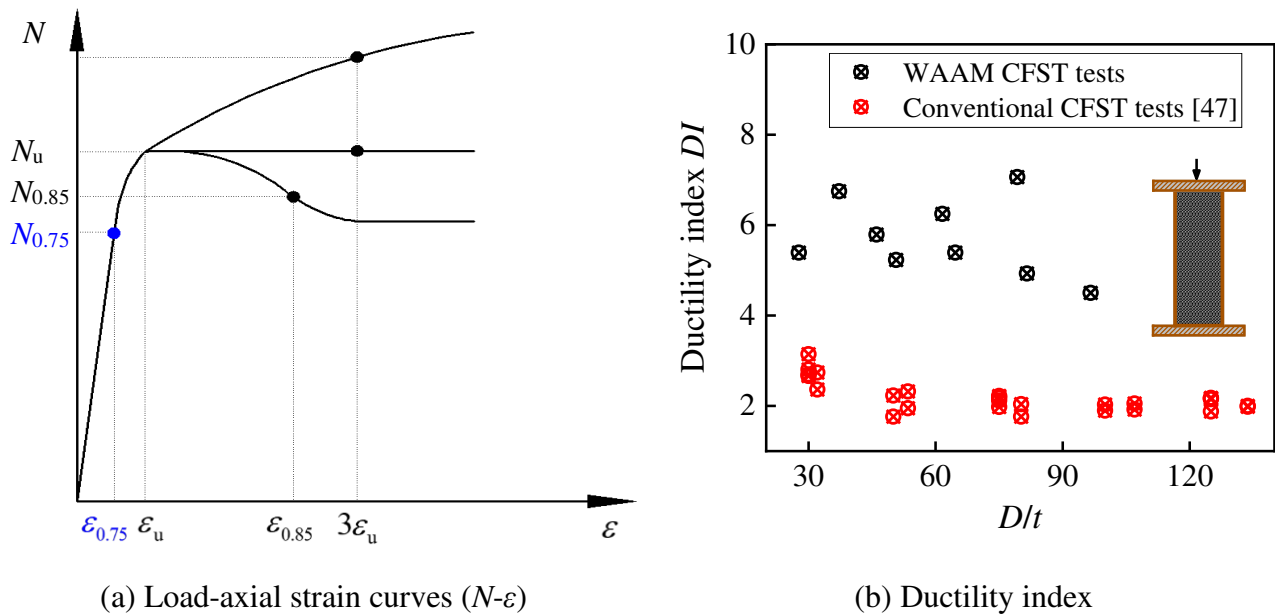


Figure 22. Load-axial strain curves and ductility indices of CFST specimens

366

**Table 7** Summary of design code expressions for predicting axial compressive resistance of CFST sections

Design code	Expression	Notes
GB 50936	$N_{u,GB} = \varphi_l N_0$	$N_0 = \begin{cases} 0.9A_c f_c (1 + 2 \frac{f_y A}{f_c A_c}) & \frac{f_y A}{f_c A_c} \leq 1 \\ 0.9A_c f_c (1 + \sqrt{\frac{f_y A}{f_c A_c}} + \frac{f_y A}{f_c A_c}) & \frac{f_y A}{f_c A_c} > 1 \end{cases}$ $\varphi_l$ : buckling reduction factor
AISC 360–16	$N_{u,AISC} = \begin{cases} P_{no} \left( 0.658 \frac{P_{no}}{P_e} \right) & \frac{P_{no}}{P_e} \leq 2.25 \\ 0.877 P_e & \frac{P_{no}}{P_e} > 2.25 \end{cases}$	$P_{no} = \begin{cases} P_p & \text{Compact} \\ P_p - \frac{P_p - P_y}{(\lambda_r - \lambda_p)^2} (\lambda - \lambda_p)^2 & \text{Non-compact} \end{cases}$ $P_p = f_y A + 0.95 A_c f_c$ ; $P_y = f_y A + 0.7 A_c f_c$ $\lambda$ , $\lambda_r$ and $\lambda_p$ : section slenderness ratio
EC4	$N_{u,EC} = \chi \left[ \eta_a f_y A + (1 + \alpha_{sc}) A_c f_c \right]$	$\alpha_{sc} = \eta_b \frac{t f_y}{D f_c}$ $\eta_a$ and $\eta_b$ : strength parameters $\chi$ : buckling reduction factor
AS 5100	$N_{u,AS} = \alpha_c \left[ \eta_2 f_y A + \left( 1 + \eta_1 \frac{t f_y}{D f_c} \right) A_c f_c \right]$	$\eta_1$ and $\eta_2$ : strength parameters $\alpha_c$ : buckling reduction factor
ACI 318	$N_{u,ACI} = f_y A + 0.85 A_c f_c$	-
BS 5400	$N_{u,BS} = 0.95 f_y A + 0.45 A_c f_{cc}$	$f_{cc} = f_{cu} + C_1 C_2 \frac{t}{D} f_y$ ; $C_1$ and $C_2$ : strength parameters
AIJ 2001	$N_{u,AIJ} = 1.27 f_y A + A_c f_c$	$L_0 / D \leq 4$



**Table 8** Comparisons of axial compression resistance predictions and experimental results for CFST specimens

Specimen ID	GB 50936		AISC 360–16		EC4		AS 5100		ACI 318		BS 5400		AIJ 2001	
	$\frac{N_{u,GB,m}}{N_{u,Exp}}$	$\frac{N_{u,GB,a}}{N_{u,Exp}}$	$\frac{N_{u,AISC,m}}{N_{u,Exp}}$	$\frac{N_{u,AISC,a}}{N_{u,Exp}}$	$\frac{N_{u,EC,m}}{N_{u,Exp}}$	$\frac{N_{u,EC,a}}{N_{u,Exp}}$	$\frac{N_{u,AS,m}}{N_{u,Exp}}$	$\frac{N_{u,AS,a}}{N_{u,Exp}}$	$\frac{N_{u,ACI,m}}{N_{u,Exp}}$	$\frac{N_{u,ACI,a}}{N_{u,Exp}}$	$\frac{N_{u,BS,m}}{N_{u,Exp}}$	$\frac{N_{u,BS,a}}{N_{u,Exp}}$	$\frac{N_{u,AIJ,m}}{N_{u,Exp}}$	$\frac{N_{u,AIJ,a}}{N_{u,Exp}}$
	D180T3L600	0.96	0.95	0.71	0.71	0.86	0.85	0.83	0.82	0.69	0.68	0.73	0.71	0.72
D240T3L600	0.97	0.96	0.72	0.72	0.87	0.86	0.88	0.87	0.70	0.69	0.73	0.71	0.70	0.69
D300T3L600	0.95	0.94	0.62	0.62	0.90	0.89	0.91	0.90	0.71	0.70	0.72	0.70	0.69	0.68
D180T6L600	1.12	1.09	0.84	0.82	1.04	1.01	0.99	0.97	0.84	0.82	0.99	0.96	0.95	0.92
D240T6L600	1.13	1.10	0.82	0.80	1.00	0.99	1.02	1.00	0.79	0.78	0.94	0.92	0.87	0.85
D300T6L600	1.10	1.08	0.79	0.78	1.01	0.99	1.02	1.00	0.77	0.75	0.90	0.88	0.82	0.80
D180T4L1200	0.98	0.96	0.62	0.60	0.94	0.92	0.81	0.79	0.75	0.74	0.76	0.74	0.80	0.79
D240T4L1200	0.99	0.98	0.68	0.67	0.91	0.90	0.85	0.84	0.74	0.73	0.75	0.74	0.76	0.75
D300T4L1200	0.95	0.93	0.63	0.62	0.87	0.86	0.85	0.84	0.71	0.70	0.71	0.70	0.71	0.69
Mean	1.02	1.00	0.71	0.70	0.93	0.92	0.91	0.89	0.74	0.73	0.80	0.78	0.78	0.76
CoV	0.070	0.068	0.113	0.112	0.069	0.065	0.087	0.084	0.061	0.056	0.129	0.124	0.108	0.103

## 371 **6. COMPARISONS AGAINST CURRENT DESIGN SPECIFICATIONS**

372 The suitability of current structural design standards for application to the studied WAAM CFST  
373 elements is assessed in this section. The axial compressive strengths of the tested specimens are  
374 compared against the strength predictions yielded by seven design codes, namely GB 50936 [52], AISC  
375 360–16 [18], EC4 [53], AS 5100 [54], ACI 318 [55], BS 5400 [56] and AIJ [57], the design formulae  
376 of which are summarised in Table 7. The average geometric properties of the specimens, as determined  
377 from the laser scans or ‘Archimedes’ measurements - see Table 4, were used for the conducted  
378 calculations. Considering that the the influence of the geometric undulations associated with WAAM  
379 inherently feature in the effective material properties of the as-built material, two different sets of  
380 material properties were considered in the design calculations: (1) the material properties from the  
381 machined coupons in the 90° direction, and (2) the material properties from the as-built coupons in the  
382 90° direction. For the machined case, in the absence of results for the 3 mm and 4 mm material, the  
383 results for the 6 mm material were used for all comparisons. For the as-built case, the mechanical  
384 properties for the corresponding nominal material thicknesses were employed (i.e. the material  
385 properties of the 3 mm thick coupons were applied to the 3 mm thick CFST specimens and the material  
386 properties of the 6 mm thick coupons were applied to 6 mm thick CFST specimens), as reported in Table  
387 6. For the 4 mm thick CFST specimens, in the absence of 4 mm thick coupon test results, the material  
388 properties of the 3 mm thick coupons were used for the calculations.

389 Comparisons between the experimental results and the strength predictions determined according  
390 to the different design codes are presented in Fig. 23 and listed in Table 8. It can be observed that use  
391 of the material properties obtained from the machined and as-built coupons leads to similar predictions  
392 of the axial compressive strengths of the examined specimens, reflecting the similarity in the two sets  
393 of material properties in the current study. As expected, use of the material properties of the as-built  
394 coupons leads to slightly more safe-sided resistance predictions since the weakening effect of the  
395 geometric undulations is accounted for.

396 The comparisons demonstrate that the resistance predictions of GB 50936 are the most accurate

397 with the mean and CoV values of  $N_{u,GB,a} / N_{u,Exp}$  being 1.00 and 0.068. The predictions yielded by EC4  
 398 and AS 5100 remain accurate and are generally safe-sided, with the mean values of  $N_{u,EC4,a} / N_{u,Exp}$  and  
 399  $N_{u,AS,a} / N_{u,Exp}$  being 0.92 and 0.89, respectively, and the corresponding CoV values being 0.065 and  
 400 0.084, respectively. All GB 50936, EC4 and AS 5100 predictions generally lay within a  $\pm 15\%$  band,  
 401 as shown Fig. 23. Finally, the resistance predictions determined according to the design equations of  
 402 AISC 360–16, ACI318, BS5400 and AIJ were found to be overly conservative.

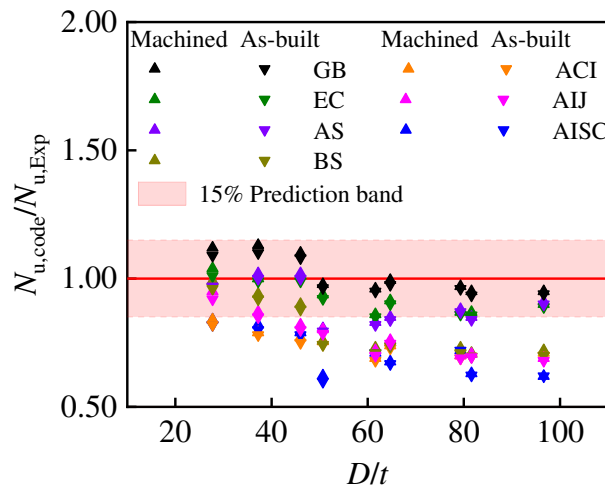


Figure 23. Comparison of resistance predictions and experimental results of CFST specimens

403 The design of WAAM CFST members will be explored further in future research, supported by the  
 404 addition of numerical simulations. In particular, the influence of the surface undulations associated with  
 405 the WAAM process will be studied.

## 406 7. CONCLUSIONS

407 An experimental investigation into the structural response of concrete-filled WAAM steel tubes has  
 408 been presented in this paper. Following determination of the geometric and material properties of the  
 409 WAAM steel, together with the strength of the infill concrete, the specimens were subjected to axial  
 410 compression tests. The key obtained results, including the load-deformation curves and failure modes,  
 411 were reported, analysed and discussed. Finally, the applicability of current design specifications to the  
 412 examined members was assessed. The main findings are summarised as follows:

413 (1) The geometric properties of the WAAM steel components were determined by hand  
 414 measurements, measurements based on Archimedes' principle and 3D laser scanning. Comparisons

415 revealed good correlation between the Archimedes' and 3D laser scan measurements. Overall, 3D laser  
416 scanning is considered to be the most suitable method for the accurate determination of the geometry of  
417 WAAM steel elements.

418 (2) Monotonic tensile coupon tests and concrete cube compression tests were conducted to obtain the  
419 material properties of the WAAM steel tubes and inner concrete, respectively. Mild anisotropy was  
420 observed for the WAAM steel, which was more pronounced for the thinner coupons.

421 (3) Nine concrete-filled WAAM steel tubular specimens were tested to investigate their mechanical  
422 behaviour under axial compression. The experimental results demonstrated that: (i) the observed failure  
423 modes are generally similar to those exhibited by CFST members comprising conventionally-produced  
424 straight seam steel tubes, (ii) the correlation between the trend of the load-end shortening curves of the  
425 examined specimens and their confinement factor is somewhat different to that of conventional CFST;  
426 this is attributed to the surface undulations of the WAAM elements, and (iii) the ductility of the  
427 examined WAAM specimens is better than that of the conventional CFST members, based on some  
428 sample comparisons.

429 (4) The axial compressive strengths of the examined CFST specimens were compared against the  
430 strength predictions yielded by current design specifications (i.e. GB 50936, AISC 360-16, EC4, AS 5100,  
431 ACI318, BS5400 and AIJ). It was shown that, provided the weakening effect of the surface undulations is  
432 taken into consideration, GB 50936, EC4 and AS 5100 offer accurate predictions of the compressive  
433 strength of concrete-filled WAAM steel tubes, within a reasonable error band (i.e.  $\pm 15\%$ ).

## 434 **Acknowledgements**

435 The authors would like to acknowledge the financial support from the National Natural Science  
436 Foundation of China (NSFC) (Grant Number: 52078249, 52208215), the Natural Science Foundation  
437 of Zhejiang Province (Grant Number: LQ22E080008) and the Centre for Balance Architecture of  
438 Zhejiang University.

## 439 **References**

- 440 [1] Gardner L. 2023. Metal additive manufacturing in structural engineering: review, advances,  
441 opportunities and outlook. *Structures*, 47, 2178–2193.
- 442 [2] ASTM. 2016. Guide for directed energy deposition of metals. F3187. West Conshohocken,  
443 PA:ASTM.
- 444 [3] ASTM. 2019. Guide for Additive manufacturing–design–directed energy deposition. F3413. West  
445 Conshohocken, PA:ASTM.
- 446 [4] Thompson MK, et al. 2016. Design for additive manufacturing: trends, opportunities,  
447 considerations, and constraints. *CIRP Annals*, 65(2):737–760.
- 448 [5] Williams SW, Martina F, Addison AC, Ding J, Pardal G, Colegrove PA. 2016. Wire+arc additive  
449 manufacturing. *Materials Science and Technology*, 32(7):641–647.
- 450 [6] Ye J, Kyvelou P, Gilardi F, Lu H, Gilbert M, Gardner L. 2021. An end–to–end framework for the  
451 additive manufacture of optimized tubular structures. *IEEE Access*, 9:165476–165489.
- 452 [7] Colegrove PA, Coules HE, Fairman JL, Martina F, Kashoob T, Mamash H, Cozzolino LD. 2013.  
453 Microstructure and residual stress improvement in wire and arc additively manufactured parts  
454 through high–pressure rolling. *Journal of Materials Processing Technology*, 213:1782–1791.
- 455 [8] Guo X, Kyvelou P, Ye J, Teh LH, Gardner L. 2022. Experimental investigation of wire arc  
456 additively manufactured steel single–lap shear bolted connections. *Thin–Walled Structures*,  
457 181:110029.
- 458 [9] Guo X, Kyvelou P, Ye J, Gardner L. 2023. Experimental investigation of wire arc additively  
459 manufactured steel T–stub connections. *Journal of Constructional Steel Research*, 211:108106.
- 460 [10] Guo X, Kyvelou P, Ye J, Teh LH, Gardner L. 2023. Experimental study of DED–arc additively  
461 manufactured steel double–lap shear bolted connections. *Engineering Structures*, 281: 115736.
- 462 [11] Haden CV, Zeng G, Carter III FM, Ruhl C, Krick BA, Harlow DG. 2017. Wire and arc additive  
463 manufactured steel: Tensile and wear properties. *Additive Manufacturing*, 16: 115–123.
- 464 [12] Kyvelou P, Huang C, Gardner L, Buchanan C. 2021. Structural testing and design of wire arc  
465 additively manufactured square hollow sections. *Journal of Structural Engineering*,  
466 147(12):04021218.
- 467 [13] Lange J, Feucht T, Erven M. 2020. 3D printing with steel–additive manufacturing for connections  
468 and structures. *Steel Construction*, 13(3), 144–153.
- 469 [14] Laghi V, Palermo M, Gasparini G, Girelli VA, Trombetti T. 2020. Experimental results for  
470 structural design of wire–and–arc additive manufactured stainless steel members. *Journal of*  
471 *Constructional Steel Research*, 16:105858.

- 472 [15]Liu YY, Ye J, Yang YZ, Quan G, Zhao WJ, Zhao Y. 2023. Experimental study on wire and arc  
473 additively manufactured steel double–shear bolted connections. *Journal of Building Engineering*,  
474 76:107330.
- 475 [16]Müller J, Grabowski M, Müller C, Hensel J, Unglaub J, Thiele K, Kloft H, Dilger K. 2019. Design  
476 and parameter identification of wire and arc additively manufactured (WAAM) steel bars for use in  
477 construction. *Metals*, 9(7): 1–19.
- 478 [17]Zhao Y, Chen Y, Wang Z, Ye J, Zhao WJ. 2023. Mechanical properties, microstructural  
479 characteristics and heat treatment effects of WAAM stainless–steel plate material. *Journal of*  
480 *Building Engineering*, 75:106988.
- 481 [18]AISC. 2016. Specification for structural steel buildings. AISC360–16. Chicago, USA:AISC.
- 482 [19]AS. 1998. Building Code of Australia Primary Referenced Standard: Steel Structures. AS4100.  
483 Homebush, Australia: AS.
- 484 [20]CEN (European Committee for Standardization). 2007. Eurocode 3: Design of Steel Structures. Part  
485 1.8: Design of Joints. EN1993–1–8. Brussels, Belgium: CEN.
- 486 [21]GB (Chinese Code). 2017. Code for Design of Steel Structures. GB 50017, Beijing, China:  
487 Standards Press of China.
- 488 [22]Kyvelou P, Slack H, Mountanou DD, Wade MA, Britton TB, Buchanan C, Gardner L. 2020.  
489 Mechanical and microstructural testing of WAAM sheet material. *Materials and Design*,  
490 192:108675.
- 491 [23]Hadjipantelis, N., Weber, B., Buchanan, C. and Gardner, L. 2022. Description of anisotropic  
492 material response of wire and arc additively manufactured thin-walled stainless steel elements.  
493 *Thin-Walled Structures*, 171, 108634.
- 494 [24]Huang, C, Meng X and Gardner L. 2022. Cross–sectional behaviour of wire arc additively  
495 manufactured tubular beams. *Engineering Structures*, 272, 114922.
- 496 [25]Kyvelou P, Buchanan C, Gardner L. 2022. Numerical simulation and evaluation of the world’s first  
497 metal additively manufactured bridge. *Structures*, 42, 405–416.
- 498 [26]Yan JJ, Chen MT, Quach WM, Yan M, Young B. 2019. Mechanical properties and cross–sectional  
499 behavior of additively manufactured high strength steel tubular sections. *Thin–Walled Structures*,  
500 144:106158.
- 501 [27]Al–Nabulsi Z, Mottram JT, Gillie M, Kourra N, Williams MA. 2021. Mechanical and X ray  
502 computed tomography characterisation of a WAAM 3D printed steel plate for structural engineering  
503 applications. *Construction and Building Materials*, 274, 121700.
- 504 [28]Huang C, Kyvelou P, Zhang R, Britton TB, Gardner L. 2022 Mechanical testing and microstructural  
505 analysis of wire arc additively manufactured steels. *Materials and Design*, 216, 110544.

- 506 [29]Huang C, Kyvelou P, Gardner L. 2023. Stress–strain curves for wire arc additively manufactured  
507 steels. *Engineering Structures*, 279, 115628.
- 508 [30]Silvestru VA, Ariza I, Vienne J, Michel L, Sanchez AMA, Angst U, Rust R, Gramazio F, Kohler  
509 M, Taras A. 2021. Performance under tensile loading of point–by–point wire and arc additively  
510 manufactured steel bars for structural components. *Materials and Design*, 205, 109740.
- 511 [31]Weber B, Meng X, Zhang R, Nitawaki M, Sagawa T, Gardner L. 2024. Tensile behaviour of  
512 WAAM high strength steel material and members. *Materials and Design*, 237, 112517.
- 513 [32]Laghi V, Palermo M, Gasparini G, Trombetti T. 2020. Computational design and manufacturing of  
514 a half–scaled 3D–printed stainless steel diagrid column. *Additive Manufacturing*, 36, 101505.
- 515 [33]Meng X, Weber B, Nitawaki M, Gardner L. 2023. Optimisation and testing of wire arc additively  
516 manufactured steel stub columns. *Thin–Walled Structures*, 189, 110857.
- 517 [34]Bruggi M, Laghi V, Trombetti T. 2021. Simultaneous design of the topology and the build  
518 orientation of wire–and–arc additively manufactured structural elements. *Computers and Structures*,  
519 242, 106370.
- 520 [35]Feucht T, Waldschmitt B, Lange J, Erven M. 2022. Additive manufacturing of a bridge in situ. *Steel  
521 Construction*, 15(2), 100–110.
- 522 [36]Kyvelou P, Spinasa A, Gardner L. 2024. Testing and analysis of optimised wire arc additively  
523 manufactured steel trusses. *Journal of Structural Engineering*, ASCE, 150(3), 04024008.
- 524 [37]Shah IH, Hadjipantelis N, Walter L, Myers RJ, Gardner L. 2023. Environmental life cycle  
525 assessment of wire arc additively manufactured structural components. *Journal for Cleaner  
526 Production*, 389, 136071.
- 527 [38]Gardner L, Li J, Meng X, Huang C, Kyvelou P. 2024. I-section steel columns strengthened by wire  
528 arc additive manufacturing concept and experiments. *Engineering Structures*, 306, 117763.
- 529 [39]Kyvelou P, Huang C, Li J, Gardner L. 2024. Residual stresses in steel I–sections strengthened by  
530 wire arc additive manufacturing. *Structures*, 60, 105828.
- 531 [40]Han LH, Zhao XL, Yang YF, Feng, JB. 2003. Experimental study and calculation of fire resistance  
532 of concrete–filled hollow steel columns. *Journal of Structural Engineering*, 129(3):346–356.
- 533 [41]Han LH, Yao GH, Zhao XL. 2005. Tests and calculations for hollow structural steel (HSS) stub  
534 columns filled with self–consolidating concrete (SCC). *Journal of Constructional Steel Research*,  
535 61:1241–1.
- 536 [42]Tao Z, Han LH, Wang ZB. 2005. Experimental behaviour of stiffened concrete–filled thin–walled  
537 hollow steel structural (HSS) stub columns. *Journal of Constructional Steel Research*, 61:962–983.
- 538 [43]Uy B, Tao Z, Han LH. 2011. Behaviour of short and slender concrete–filled stainless steel tubular  
539 columns. *Journal of Constructional Steel Research*, 67(3):360–378.

- 540 [44] Wang F, Young B, Gardner L. 2020. CFDST sections with square stainless steel outer tubes under  
541 axial compression: Experimental investigation, numerical modelling and design. *Engineering*  
542 *Structures*, 207, 110189.
- 543 [45] Liang QQ, Uy B, Liew JYR. 2006. Nonlinear analysis of concrete-filled thin-walled steel box  
544 columns with local buckling effects. *Journal of Constructional Steel Research*, 62(6):581–591.
- 545 [46] Xiong MX, Xiong DX, Liew JYR. 2017. Axial performance of short concrete filled steel tubes with  
546 high-and ultra-high-strength materials. *Engineering Structures*, 136:494–510.
- 547 [47] Yu Q, Tao Z, Wu YX. 2008. Experimental behaviour of high-performance concrete-filled steel  
548 tubular columns. *Thin-Walled Structures*, 46:362–370.
- 549 [48] Song SS, Chen J, Ye J, Quan G, Wang Z, Xiao JZ. 2024. Experimental study on the interfacial bond  
550 behaviour of circular concrete-filled WAAM steel tubes. *Journal of Building Engineering*,  
551 82:108171.
- 552 [49] Xu F, Chen J, Jin WL. 2014. Experimental investigation of thin-walled concrete-filled steel tube  
553 columns with reinforced lattice angle. *Thin-Walled Structures*, 84:59-67.
- 554 [50] Xu F, Chen J, Guo Y, Ye Y. 2019. Innovative design of the world's tallest electrical transmission  
555 towers. *Proceedings of the Institution of Civil Engineers – Civil Engineering*, 172(5): 9–16.
- 556 [51] Song SS, Chen J, Quan G, Ye J, Zhao Y. 2024. Numerical analysis and design of concrete-filled  
557 wire arc additively manufactured steel tube under axial compression. *Engineering Structures*,  
558 301:117294.
- 559 [52] GB (Chinese Code). 2014. Technical code for concrete-filled steel tubular structures. GB 50936.  
560 Beijing, China: Standards Press of China.
- 561 [53] CEN (European Committee for Standardization). 2004. Eurocode 4: Design of composite steel and  
562 concrete structures–Part 1–1: General rules and rules for buildings. EN1994–1–1. Brussels,  
563 Belgium: CEN.
- 564 [54] AS. 2004. Bridge design Part 6: Steel and composite construction. AS 5100. Sydney, Australia: AS.
- 565 [55] ACI. 2002. Building code requirements for reinforced concrete and commentary. ACI 318R–02.  
566 Detroit, American: AIC.
- 567 [56] BS. 2000. Steel, concrete and composite bridges: code of practice for design of composite bridges  
568 Part 5. BS 5400. London, British: BS.
- 569 [57] AIJ (Japanese Code). 1997. Recommendations for design and construction of concrete filled steel  
570 tubular structures. AIJ. Japan: AIJ.
- 571 [58] Rhinoceros 3D, Robert McNeel & Associates, 2017.
- 572 [59] Ye J, Liu YY, Yang YZ, Wang Z, Zhao O, Zhao Y. 2023. Testing, analysis and design of wire and  
573 arc additively manufactured steel bolted connections. *Engineering Structures*, 296:116939.



- 574 [60] Ibrahim A, Mahmoud E, Yamin M, Patibandla VC. 2014. Experimental study on Portland cement  
575 pervious concrete mechanical and hydrological properties. *Construction and Building Materials*,  
576 50:524–529.
- 577 [61] Park SB, Tia M. 2004. An experimental study on the water-purification properties of porous  
578 concrete. *Cement and Concrete Research*, 34(2):177–184.
- 579 [62] Geomagic Wrap, 3D Systems Inc, 2017.
- 580 [63] GB (Chinese Code). 2010. *Metallic materials–Tensile testing–Part 1: Method of test at room*  
581 *temperature*. GB/T 228.1. Beijing, China: Standards Press of China.
- 582 [64] GB (Chinese Code). 2002. *Test method for mechanical properties of ordinary concrete*. GB/T 50081.  
583 Beijing, China: Standards Press of China.
- 584 [65] CEB–FIP Model Code 2010, *Fib model code for concrete structures 2010*, International Federation  
585 *Bedton (FIB)*, Lausanne, Switzerland, 2012.
- 586 [66] Song SS, Liu X, Chen J, Ye CH, Liu JDR, Liu CB. 2022. Compressive behaviour of corroded thin-  
587 walled circular section steel stub columns. *Thin-Walled Structures*, 180:109794.
- 588 [67] Song SS, Xu F, Chen J, Qin FJ, Huang Y, Yan X. 2022. Feasibility and performance of novel  
589 tapered iron bolt shear connectors in demountable composite beams. *Journal of Building*  
590 *Engineering*, 53:104528.
- 591 [68] Aslani F, Uy B, Tao Z, Mashiri F. 2015. Behaviour and design of composite columns incorporating  
592 compact high-strength steel plates. *Journal of Constructional Steel Research*, 107:94–110.
- 593 [69] Schneider SP. 1998. Axially loaded concrete-filled steel tubes. *Journal of Structural Engineering*,  
594 124(10):1125–38.
- 595 [70] Uenaka K. 2014. Experimental study on concrete-filled elliptical/oval steel tubular stub columns  
596 under compression. *Thin-Walled Structures*, 78:131–137.
- 597 [71] Uy B. 2000. Strength of concrete filled steel box columns incorporating local buckling. *Journal of*  
598 *Structural Engineering*, 126(3):341–52.
- 599 [72] Ding FX, Luo L, Zhu J, Wang LP, Yu ZW. 2018. Mechanical behavior of stirrup-confined  
600 rectangular CFT stub columns under axial compression. *Thin-Walled Structures*, 124:136–50.
- 601 [73] Chen ZP, Liu DY, Liang YH, Zhou J. Experimental investigation on axial compression performance  
602 of spiral reinforcement ocean concrete-filled stainless steel tube columns. *Journal of Building*  
603 *Structures* 2022; DOI:10.14006/j.jzjgxb.2022.0401. (in Chinese)